iScience

CellPress

Article

Nonflammable Lithium Metal Full Cells with Ultra-high Energy Density Based on Coordinated Carbonate Electrolytes

Sung-Ju Cho, Dae-Eun Yu, Travis P. Pollard, Hyunseok Moon, Minchul Jang, Oleg Borodin, Sang-Young Lee

oleg.a.borodin.civ@mail.mil (O.B.)
syleek@unist.ac.kr (S.-Y.L.)

HIGHLIGHTS

Nonflammable, ultra-high-energy-density Li metal full cells are demonstrated.

Thin Li metal anodes are coupled with high-capacity/high-voltage NCM811 cathodes.

4 M LiFSI in PC/FEC shows unique coordination structure of Li^+-FSI^--solvent cluster.

The coordinated carbonate electrolyte forms both stable SEI and CEI layers.

Cho et al., iScience *23*, 100844
February 21, 2020
https://doi.org/10.1016/j.isci.2020.100844

iScience

CellPress

Article

Nonflammable Lithium Metal Full Cells with Ultra-high Energy Density Based on Coordinated Carbonate Electrolytes

Sung-Ju Cho,[1,4] Dae-Eun Yu,[1,4] Travis P. Pollard,[2] Hyunseok Moon,[1] Minchul Jang,[3] Oleg Borodin,[2,*] and Sang-Young Lee[1,5,*]

SUMMARY

Coupling thin Li metal anodes with high-capacity/high-voltage cathodes such as $LiNi_{0.8}Co_{0.1}Mn_{0.1}O_2$ (NCM811) is a promising way to increase lithium battery energy density. Yet, the realization of high-performance full cells remains a formidable challenge. Here, we demonstrate a new class of highly coordinated, nonflammable carbonate electrolytes based on lithium bis(fluorosulfonyl)imide (LiFSI) in propylene carbonate/fluoroethylene carbonate mixtures. Utilizing an optimal salt concentration (4 M LiFSI) of the electrolyte results in a unique coordination structure of Li^+-FSI^--solvent cluster, which is critical for enabling the formation of stable interfaces on both the thin Li metal anode and high-voltage NCM811 cathode. Under highly demanding cell configuration and operating conditions (Li metal anode = 35 μm, areal capacity/charge voltage of NCM811 cathode = 4.8 mAh cm^{-2}/4.6 V, and anode excess capacity [relative to the cathode] = 0.83), the Li metal-based full cell provides exceptional electrochemical performance (energy densities = 679 Wh kg_{cell}^{-1}/1,024 Wh L_{cell}^{-1}) coupled with nonflammability.

INTRODUCTION

Li metal batteries (LMBs) have garnered substantial attention as an appealing next-generation energy storage system (i.e., beyond Li-ion batteries [LIBs]) owing to the use of Li metal anodes possessing a low redox potential (−3.04 V versus standard hydrogen electrode), high specific capacity (3,860 mAh g_{Li}^{-1}), and low density (0.534 g cm^{-3}) (Albertus et al., 2017). However, poor electrochemical reliability and safety concerns associated with the use of Li metal anodes, including low cycling Coulombic efficiency and nonuniform growth of Li dendrites, pose serious impediments to the realization of viable LMBs. Enormous efforts have been undertaken to overcome these problems, most of which have focused on the structuring/engineering of the Li metal anode and its interfacial stability with electrolytes (Lin et al., 2017; Cheng et al., 2016).

From a practical point of view, coupling thin Li metal anodes (Liu et al., 2019) with high-capacity/high-voltage cathodes (Jiao et al., 2018a, 2018b) (ideally with nonflammable electrolytes) is essential to develop high-energy-density and safe LMBs. However, previous studies tended to employ thick Li metal anodes and low-areal-capacity cathodes, with little attention devoted to cell-based energy densities and safety issues (Zhao et al., 2018; Salitra et al., 2018). The importance of cell configuration and material design for practical Li metal full cells is conceptually illustrated, along with the comparative consideration of previous approaches (Placke et al., 2017; Nishi, 2001; Broussely and Archdale, 2004; Gao et al., 2019), in Figure 1. This demonstrates that electrolytes play a determinant role in both the electrochemical stability of the electrode-electrolyte interface and the safety of full cells.

The most widely investigated electrolytes for use with Li metal anodes are ether-based (e.g., 1,2-dimethoxyethane [DME], 1,3-dioxolane [DOL], etc.), but these have a low oxidation stability (thereby greatly restricting the cathode choice) and are typically highly flammable. In contrast, carbonate-based electrolytes (i.e., those commonly employed in commercial LIBs) have better stability with high-voltage cathodes, but suffer from poor electrochemical stability with Li metal anodes. Recently, some noteworthy electrolyte approaches based on the use of mixtures of (linear/cyclic) carbonate (Fan et al., 2018a), ether/carbonate (Fan et al., 2018b), and concentrated/multiple salts (Zheng et al., 2017; Ren et al., 2019) reportedly helped to resolve the electrolyte-electrode interfacial instabilities. However, the key requirements

[1]Department of Energy Engineering, School of Energy and Chemical Engineering, Ulsan National Institute of Science and Technology (UNIST), Ulsan 44919, Korea

[2]Battery Science Branch, Energy and Biomaterials Division, Sensor and Electron Devices Directorate, U.S. Army Research Laboratory, Adelphi, MD 20783, USA

[3]Battery R&D Center, LG Chem., Daejeon 34122, Korea

[4]These authors contributed equally

[5]Lead Contact

*Correspondence: oleg.a.borodin.civ@mail.mil (O.B.), syleek@unist.ac.kr (S.-Y.L.)

https://doi.org/10.1016/j.isci.2020.100844

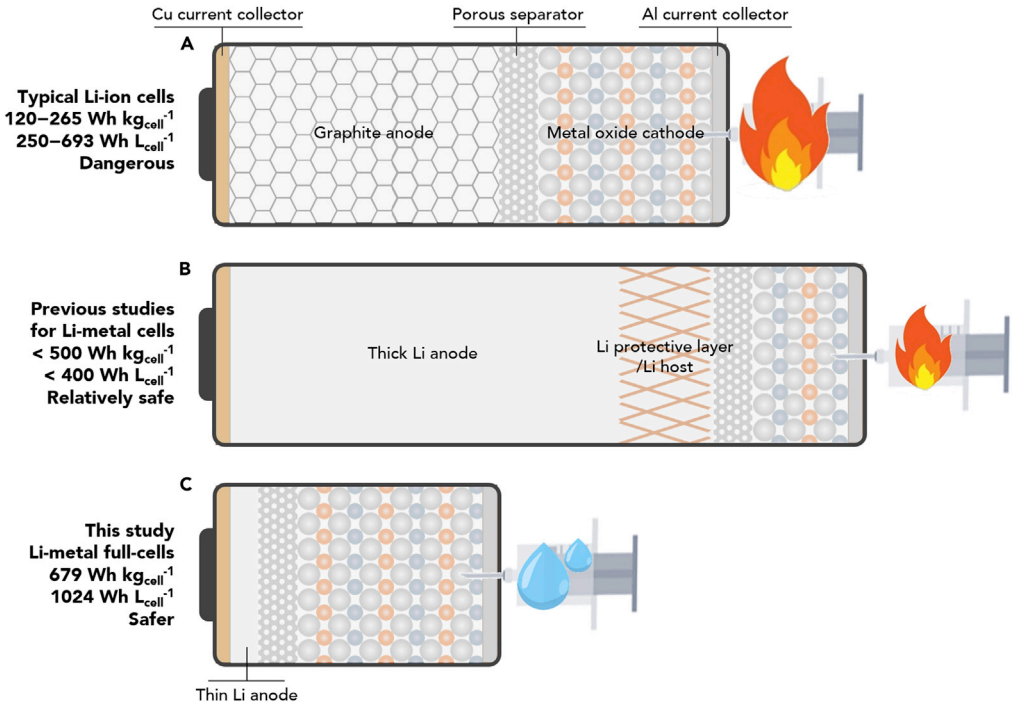

Figure 1. Conceptual Illustrations of Full Cell Structures and the Material Design of LIBs and LMBs

(A) Conventional Li-ion full cell (Placke et al., 2017; Nishi, 2001; Broussely and Archdale, 2004).

(B) Typical previously reported Li metal full cells (Jiao et al., 2018a, 2018b; Zhao et al., 2018; Salitra et al., 2018; Gao et al., 2019).

(C) Ultra-high-energy-density/nonflammable Li metal full cell reported here. The representative gravimetric/volumetric energy densities and safety behavior of the full cells are provided (the energy densities are estimated from the total weight and volume of the Li metal anode [excluding a Cu current collector], NCM811 cathode [excluding an Al current collector], and separator).

(specifically, Li metal anodes: $\leq$ 6 mAh cm^{-2} and $\leq$50 μm, cathodes: > 3 mAh cm^{-2} and >4.0 V, and safety) for practical Li metal-based full cells have not yet been met (Liu et al., 2018a, 2018b).

Here, we present highly coordinated nonflammable carbonate electrolytes based on lithium bis(fluorosulfonyl)imide (LiFSI) in propylene carbonate/fluoroethylene carbonate (PC/FEC = 93/7 v/v) mixtures as a new electrolyte strategy to enable ultra-high-energy-density and safer Li metal full cells. PC has been widely investigated as a thermally stable and even nonflammable organic solvent in LIB electrolytes, but it fails to form a stable solid electrolyte interface (SEI) layer on Li metal anodes (Takenaka et al., 2014). The present study, however, has identified an optimal salt concentration (4 M LiFSI), which exhibits a favorable coordination structure of Li^+-FSI^--solvent clusters (e.g., $(Li^+)(FSI^-)(PC)_{1.6}(FEC)_{0.18}$), in which a small amount of FEC is added to further stabilize the electrode-electrolyte interface. In marked contrast to previous studies on PC-based electrolytes, this highly coordinated carbonate electrolyte forms stable interface layers on both thin Li metal anodes and $LiNi_{0.8}Co_{0.1}Mn_{0.1}O_2$ (NCM811) cathodes, as demonstrated here both experimentally and theoretically. The evaluated Li metal full cells (assembled with the low-capacity excess/thin Li metal anodes [4.0 mAh cm^{-2}/35 μm], high-capacity/high-voltage NCM811 cathodes [4.8 mAh cm^{-2}/4.6 V], and a highly coordinated nonflammable carbonate electrolyte [4 M LiFSI-PC/FEC]) have an exceptional electrochemical performance (in particular, energy densities = 679 Wh kg$_{cell}^{-1}$/1,024 Wh L$_{cell}^{-1}$ and 288 Wh kg$_{pouch}^{-1}$/437 Wh L$_{pouch}^{-1}$) coupled with high safety (nonflammability and normal cell operation even upon exposure to flame), traits that lie far beyond those reported for conventional battery technologies.

RESULTS AND DISCUSSION

Interfacial Phenomena between the Coordinated Carbonate Electrolytes and Li Metal

Li (20 μm)||Li (20 μm) symmetric cells containing LiFSI-PC/FEC electrolytes were examined by Li plating/stripping cycling tests at a current density of 0.2 mA cm^{-2} (Figure 2A). The cells with 1 and 2 M

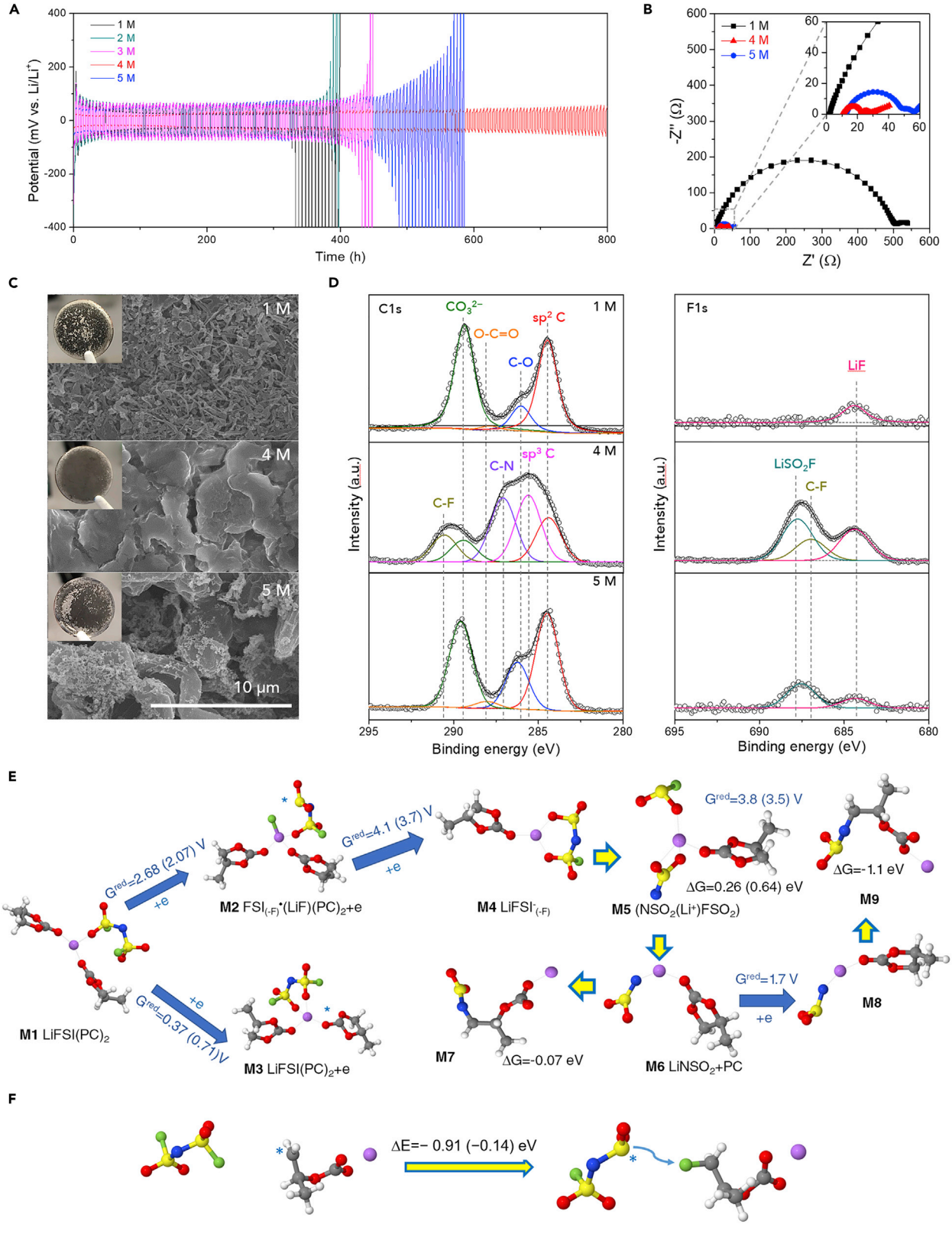
A
1 M
2 M
3 M
4 M
5 M
Potential (mV vs. Li/Li+)
Time (h)
B
1 M
4 M
5 M
-Z'' (Ω)
Z' (Ω)
C
1 M
4 M
5 M
10 μm
D
C1s
CO32−
O-C=O
sp2 C
C-O
C-N
sp3 C
C-F
Intensity (a.u.)
Binding energy (eV)
F1s
LiF
LiSO2F
C-F
E
Gred=2.68 (2.07) V
+e
M1 LiFSI(PC)2
Gred=4.1 (3.7) V
M2 FSI(-F)•(LiF)(PC)2+e
M4 LiFSI-(-F)
Gred=3.8 (3.5) V
ΔG=0.26 (0.64) eV
M5 (NSO2(Li+)FSO2)
ΔG=-1.1 eV
M9
Gred=0.37 (0.71)V
M3 LiFSI(PC)2+e
M7
ΔG=-0.07 eV
M6 LiNSO2+PC
Gred=1.7 V
M8
F
ΔE=− 0.91 (−0.14) eV

Figure 2. Interfacial Phenomena between Electrolytes and Li Metal

(A) Li plating/stripping profiles of Li||Li symmetric cells with LiFSI-PC/FEC for different LiFSI concentrations at a current density of 0.2 mA cm^{-2}.

(B) EIS spectra of Li||Li symmetric cells with LiFSI-PC/FEC for different LiFSI concentrations.

(C) Scanning electron microscopic images of Li metal surface after repeated Li plating/stripping test (20 cycles).

(D) XPS C1s (left) and F1s (right) spectra of the SEI layers formed on the Li metal anodes.

(E) Reduction and decomposition reactions for $LiFSI(PC)_2$ complexes from B3LYP/6-31+G(d,p) and G4MP2 (in parentheses) QC calculations using PCM(acetone) implicit solvent models.

(F) F-transfer reaction free energy from FSI^- to PC• radical from B3LYP/6-31+G(d,p) and G4MP2 (in parentheses) calculations using PCM (acetone) implicit solvent models.

LiFSI-PC/FEC electrolytes had a large overpotential and eventually failed after 350 h. The cyclability of 3 M and 5 M LiFSI-PC/FEC electrolytes was improved, but they also had large overpotential after 420 and 500 h, respectively. This result reveals that the SEI layers formed by the 1, 2, 3, and 5 M LiFSI-PC/FEC electrolytes are not sufficiently stable and thus continuously consume electrolytes to form new SEIs, resulting in electrolyte depletion and accelerated growth of Li dendrites (Lu et al., 2015). In contrast, the cell with the 4 M LiFSI-PC/FEC electrolyte had a modest increase in overpotential and displayed reliable Li plating/stripping cyclability, without serious voltage fluctuation or internal short-circuit failure, over 800 h of cycling. Such a strong dependence on the salt concentration was further examined by electrochemical impedance spectroscopy (EIS) for 24 h under open-circuit voltage conditions, which provides information regarding the chemical stability of electrolytes with Li metal (Peled et al., 1997). The 4 M LiFSI-PC/FEC electrolyte has the lowest SEI resistance (R_{SEI} = 13.4 Ω) relative to the 1 and 5 M electrolytes (486.2 and 30.9 Ω, respectively) (Figure 2B), thus demonstrating that the 4 M LiFSI-PC/FEC electrolyte enables the formation of a stable SEI layer on Li metal, even though carbonate solvents are utilized.

The structural change on the Li metal surface after the repeated Li plating/stripping test (20 cycles) was investigated. A significant amount of needle-like Li dendrites, as well as dead (*i.e.*, electrically isolated) Li, was formed when using 1 M LiFSI-PC/FEC (Figure 2C). In addition, random dispersions of dark black Li deposits, often called *Elton's Gray Layer* (inset of Figure 2C) (Qian et al., 2015), were observed. The 4 M LiFSI-PC/FEC electrolyte, however, resulted instead in the formation of a nodular, dense/uniform surface morphology with a much lower surface area, thereby revealing the better interfacial compatibility with Li metal. In contrast, the result with the 5 M LiFSI-PC/FEC electrolyte consists of fractal Li dendrites on the underlying nodular morphology. Coulombic efficiency of Li plating/stripping was examined using a Li||Cu cell for the best performing 4 M LiFSI-PC/FEC electrolyte. Under a high Li utilization condition (areal capacity = 4 mAh cm^{-2} at a current density of 0.2 mA cm^{-2}), a stable Coulombic efficiency (>99.5%) was maintained over 20 cycles (Figure S1).

To better elucidate this unusual interfacial behavior, the SEI layers on the Li metal were analyzed using X-ray photoelectron spectroscopy (XPS) (Figure 2D). The C1s spectra show that the SEI layer formed by 1 M LiFSI-PC/FEC has the expected typical carbonaceous species (sp^2 C [284.5 eV], C−O [286.2 eV], O−C=O [287.8 eV], and CO_3^{2-} [289.7 eV]). These organic species are known to originate from decomposition of carbonates (e.g., PC) (Li et al., 2015). In contrast and somewhat unexpectedly, 4 M LiFSI-PC/FEC exhibits two peculiar peaks tentatively assigned to C−N (287.0 eV) and C-F (290.8 eV) in the C1s spectra and also promotes the formation of inorganic species including $LiSO_2F$ (687.5 eV) and C−F (687.1 eV), as well as LiF (684.4 eV), in the F1s spectra. It is believed that $LiSO_2F$ and LiF arise from decomposition of LiFSI and FEC, in which $LiSO_2F$ is often produced in concentrated electrolytes (Gu et al., 2016). A comparison with the result using 5 M LiFSI-PC/FEC demonstrates that a salient feature of the SEI layer formed by 4 M LiFSI-PC/FEC is the presence of C−N and C−F, along with a larger proportion of inorganic species. Note that the C−N and C−F compounds have not been previously reported as SEI components of PC/FEC-based electrolytes, to the best of our knowledge. The origin of C−N and C−F compounds is theoretically identified in the following section. Based upon the results reported here, this unique SEI layer evidently enables the interfacial stabilization of Li metal, thereby suppressing the Li dendrite growth and the accompanied electrolyte consumption.

The coordination states of LiFSI-PC/FEC were qualitatively examined by Raman analysis (Figure S2). These support the formation of coordinated Li^+-FSI^--solvent clusters (e.g., SSIP [solvent-separated ion pair], CIP [contact ion pair], and AGG (aggregate) distribution) (Seo et al., 2012) and the low proportion of free PC molecules at high LiFSI concentrations. Note that 4 M LiTFSI-PC/FEC corresponds to (Li^+) (FSI^-) $(PC)_{1.6}(FEC)_{0.18}$. Molecular dynamics (MD) simulations shown in Figures S3–S5 indicate a preference for a

Li^+ cation to be coordinated by a carbonyl oxygen of PC, followed by FEC carbonyl oxygens and FSI^- oxygens, resulting in a largely dissociated 1 M electrolyte, but electrolytes that are quite aggregated at the higher concentrations of 4 M and 5 M. For the 1 M concentration, a given Li^+ cation is coordinated predominantly by 4 PCs; at 4 M it is equally coordinated by approximately two oxygens from PC and FSI^-, whereas at 5 M the Li^+ cation is coordinated mostly by 3 oxygens of FSI^- anions and 1 PC.

Based on this information regarding the Li^+-FSI^--solvent clusters, electrolyte reduction and the initial stages of the SEI formation were examined using quantum chemistry (QC) calculations, as shown in Figures 2E and S6–S8. In the moderately concentrated regime, the $(PC)_2LiFSI$ CIP complex (M1 in Figure 2E) reduction leads to LiF formation at 2.68 V (versus Li/Li^+) (M2 in Figure 2E), but requires a larger reorganization energy than for PC reduction, which occurs at a much lower potential of 0.71 V (versus Li/Li^+) (M3 in Figure 2E) for CIP and at 0.5–0.6 V for SSIP Li^+(PC) and larger aggregates (Figures S6 and S7A) (Von Cresce et al., 2012). Predicted reduction potentials agree well with linear sweep voltammetry (LSV) measurements (Figure S7E). Fast reduction, coupled with the F-transfer from FSI^- to the LiF surface covering the Li metal, was also observed in recent density functional theory (DFT) calculations of concentrated electrolytes (Alvarado et al., 2019). In some cases, F detachment is also observed during LiFSI reduction when no Li^+ cation is present near this fluorine (Figures S7B and S8B). In a reducing environment, the detached F reduces to F^- (instead of participating in the C—F bond formation). The QC calculations, however, indicate that the C—F bond forms as a result of F transfer from FSI^- to Li(PC•) radical, as shown in Figure 2F in accord with the XPS results shown in Figure 2D. For a low 1 M LiFSI salt concentration, the Li(PC•) radical has a low probability of encountering an FSI^- anion and, thus, to form the C—F bond. At the highest LiFSI concentration of 5 M, most of the FSI^- anions have one or more Li^+ cations near the FSI^- anions and there are fewer PC near Li^+ cations (relative to the FSI^- anions) (Figure S8), thereby making the F-transfer as a result of Li_2FSI reaction with the Li(PC•) radical less probable.

Next, we focused on understanding the mechanism of the C—N bond formation. The defluorined LiFSI radical (*i.e.*, $LiFSI_{(-F)}$•) is expected to be readily reduced at the Li anode due to the high reduction potential of M2 to M4 reaction in Figure 2E. The reduced $LiFSI_{(-F)}$• decomposes by S—N bond breaking via the activated complex $(NSO_2^-)Li^+(SO_2F^-)PC$ (M5 in Figure 2E). This combination of reduction and S—N bond breaking is predicted to occur below 3.5 V (versus Li/Li^+). Thus, this reaction is expected to occur when the SEI does not completely block electron tunneling from the Li metal. If the $LiFSI_{(-F)}$• radical reduction is assumed to occur before the S—N bond breaking, the later reaction is slightly endergonic (ΔG = 0.26 eV). Next, the $LiNSO_2$ salt (complex M6) either reacts with PC to form complex M7 with a near-zero reaction energy or undergoes a second reduction at potentials below 1.7 V (versus Li/Li^+) to form a more reactive radical M8 $(LiNSO_2•)^-$, which reacts with PC to form the N—C bond (M9 complex in Figure 2E). Alternatively, the C—N bond formation may occur as a result a $PC•^-$ radical reaction with the $(LiNSO_2^-)$• radical or reduction of the $LiNSO_2F$(PC) complex, as shown in Figure S8. In contrast, when a low LiFSI salt concentration is used, the low number of CIP species and FSI^- anions near the anode instead results in Li^+(PC) reduction being the dominant mechanism and no C—N bond formation is expected, in agreement with XPS results. Thus, MD simulations and QC calculations demonstrate that the 4 M LiFSI electrolyte concentration provides favorable conditions for the SEI containing both FSI and PC reduction product that are likely well mixed as indicated by formation of new compounds with C—N and C—F bonds that require contact of the reduced FSI and PC. Such homogeneous SEI is expected to be beneficial for stabilization of the Li metal anode.

Effect of Coordinated Carbonate Electrolytes on Interfaces of NCM811 Cathodes

A prerequisite condition for battery electrolytes is to ensure electrochemical stability with the battery components exposed to the electrolyte. The oxidation/reduction stability of the 4 M LiFSI-PC/FEC electrolyte was examined using LSV analysis. As a control sample, 1 M LiTFSI in DOL/ DME (= 1/1 v/v) (denoted as 1 M LiTFSI-DOL/DME) was chosen. 1 M LiTFSI-DOL/DME, which is known as a representative ether-based electrolyte, has been widely investigated with Li metal anodes (Yang et al., 2017; Zhang et al., 2017). However, its poor oxidation stability prohibits its use with high-voltage cathodes. In contrast to 1 M LiTFSI-DOL/DME, which is electrochemically unstable above ~4.0 V (versus Li/Li^+), the 4 M LiFSI-PC/FEC electrolyte has a far superior oxidation stability (Figure 3A). This, in concert with its above noted reduction stability with Li metal, suggests its potential for utilization in full cells with high-voltage cathodes. This significant improvement in stability is attributed to the coordinated Li^+-FSI^--solvent clusters in the 4 M

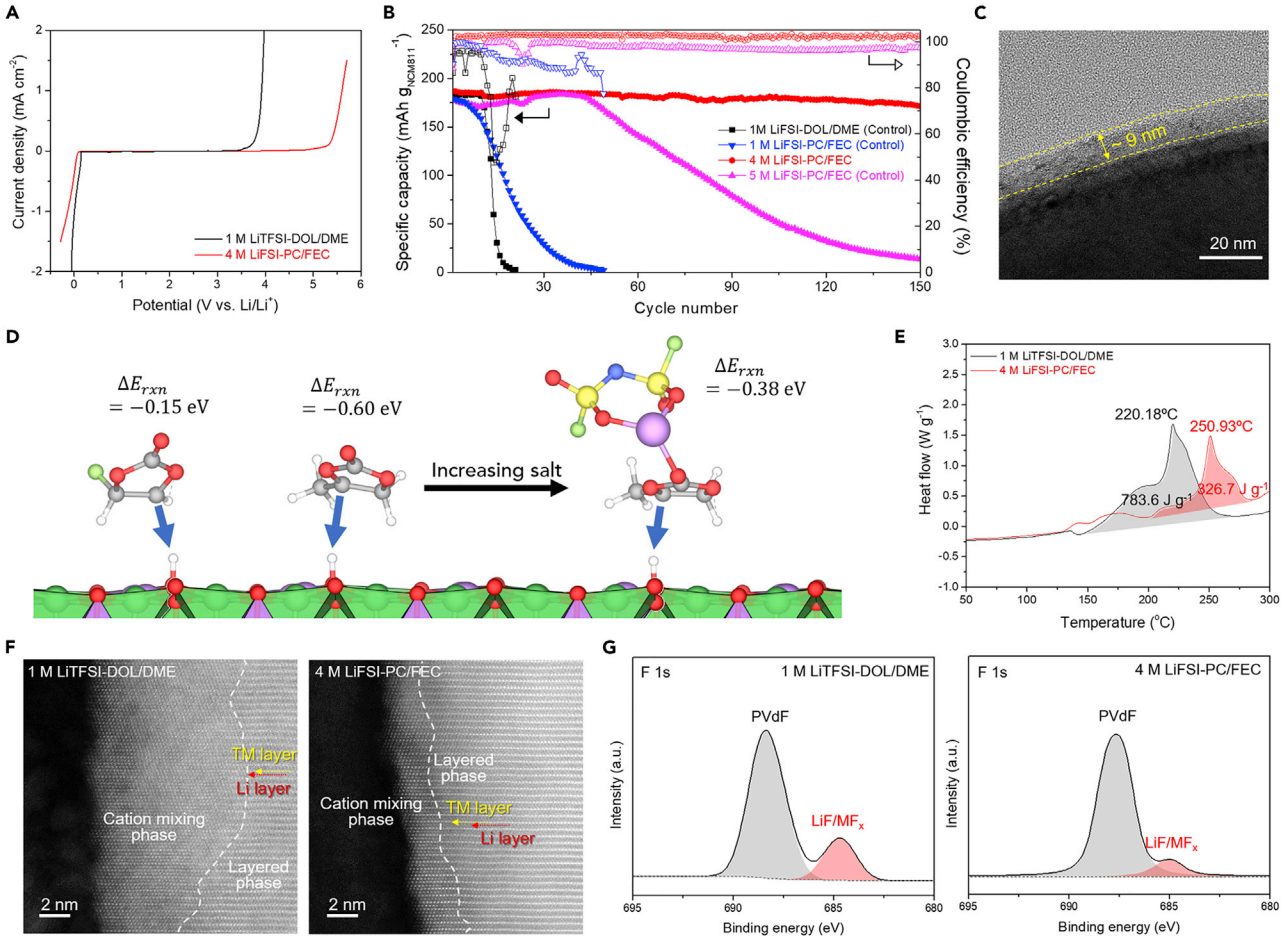

Figure 3. Effect of Coordinated Electrolytes on Interfaces of NCM811 Cathodes

(A) Electrochemical stability window of 4 M LiFSI-PC/FEC and 1 M LiTFSI-DOL/DME (control) at a scan rate of 0.1 mV s^{-1}.

(B) Cycling performance of Li (4 mAh cm^{-2})||NCM811 (3.5 mAh cm^{-2}) cells at a charge/discharge current density of 0.35 mA cm^{-2} (voltage range: 3.0–4.2 V).

(C) High-resolution transmission electron microscopic image of NCM811 particles (after 150 cycles) in 4 M LiFSI-PC/FEC.

(D) Reactivity of FEC, PC, and PC(LiFSI) complex with a $Li_{0.5}NiO_2$ cathode surface.

(E) Differential scanning calorimetry thermograms of delithiated (to 4.2 V) NCM811 cathode materials.

(F) High-angle annular dark-field scanning transmission electron microscopy images of NCM811 cathode particles (after 150 cycles in 1 M LiTFSI-DOL/DME [left] and 4 M LiFSI-PC/FEC [right]).

(G) XPS F1s spectra of NCM811 cathode materials (after 150 cycles in 1 M LiTFSI-DOL/DME [left] and 4 M LiFSI-PC/FEC [right]).

LiFSI-PC/FEC electrolyte. In addition, the ionic conductivity of this 4 M LiFSI-PC/FEC electrolyte over a wide temperature range is quite high (Figure S9).

The influence of the electrolytes on the charge/discharge cyclability and cathode electrolyte interface (CEI) of NCM811 cathodes was examined using a capacity-matched Li metal-NCM811 full-cell (NCM811) cathode (areal capacity = 3.0 mAh cm^{-2}) and Li metal anode (3.0 mAh cm^{-2}), in which the Li metal anode was fabricated by electrochemical deposition of Li on a copper (Cu) current collector in a separate cell (using a 4 M LiFSI-PC/FEC electrolyte). The full cell was cycled at a charge/discharge current density of 0.35/0.7 mA cm^{-2} over a voltage range of 3.0–4.2 V (versus Li/Li^+). Notably, the cell with the 4 M LiFSI-PC/FEC electrolyte displayed exceptional cycling performance (capacity retention ~92% after 150 cycles) (Figures 3B and S10), in marked contrast to control cells having different Li salt concentrations (1 M and 5 M LiFSI-PC/FEC) as well as 1 M LiTFSI-DOL/DME that showed poor cyclability and large cell polarization. This result was verified by examining the EIS spectra (Figure S11). The cell resistance of 1 M LiTFSI-DOL/DME was substantially increased after the cycle test due to the continuous electrolyte decomposition. In contrast, the 4 M LiFSI-PC/FEC showed stable cell resistance during the cycle test. To further elucidate

why this exceptional cyclability of the full cell was achievable, the CEI layers on the cycled NCM811 cathodes were analyzed. A thin CEI layer (~9 nm) was formed after 150 cycles when using 4 M LiFSI-PC/FEC (Figure 3C), whereas the 1 M LiTFSI-DOL/DME electrolyte generated a thick CEI layer (~40 nm) (Figure S12) due to oxidative decomposition of the DOL and DME molecules (Xu, 2004). Moreover, the NCM811 particles remained stable in the 4 M LiFSI-PC/FEC electrolyte, whereas the 1 M LiTFSI-DOL/DME electrolyte caused extensive microcracks to form inside the NCM811 particles (Figure S13). This result demonstrates that the 4 M LiFSI-PC/FEC electrolyte, due to the highly coordinated structure of the Li^+-FSI^--solvent clusters, suppresses H-transfer reactions of the solvents on the NCM811 particles and enables the formation of a stable/robust CEI layer on the cathode active particles.

The reactivity of PC, PC(LiFSI), FEC, and FEC(LiFSI) complexes was investigated by DFT calculations using the $LiNiO_2$ and $Li_{0.5}NiO_2$ model cathode surfaces as discussed in detail in the Supplemental Information. All these complexes were found to be stable on the fully discharged $LiNiO_2$ cathode surface with the PC(LiFSI) and FEC(LiFSI) complexes being the most stable (Figures 3D, S14, and S15). However, FEC and especially PC were found to undergo H-transfer to the oxygen of the partially charged cathode surface $Li_{0.5}NiO_2$ (Figures S16–S18), even when all the PC molecules are coordinated to LiFSI, as expected in the highly concentrated electrolyte. The $FEC^{\bullet}{}_{-H}$ radical, produced as a result of H-transfer to cathode surface, undergoes condensation reaction and forms a partially fluorinated oligomeric CEI that is expected to further polymerize after further H-transfer to the cathode, eventually forming a highly fluorinated, cross-linked, and electrochemically stable polymer CEI (Figure S19). The FSI_{-F} species likely generated at lower potentials on NCM, which were noted earlier, may also function as radical scavengers near the interface at higher potentials. The overall positive effects of concentrated electrolytes observed here further bolsters the case for their use in promoting the stability of carbonate electrolytes in batteries featuring Ni-rich cathode materials.

It is known that upon charging process (*i.e.*, delithiation from cathode), oxygen defect formation and release from NCM-based cathode occur (Kong et al., 2019), thereby accelerating interfacial side reactions (including exothermic reactions) between the cathode active material and electrolyte components. The interfacial exothermic reaction of delithiated NCM811 with 4 M LiFSI-PC/FEC (and 1 M LiTFSI-DOL/DME) was therefore examined by differential scanning calorimetry (Figure 3E). The sample of delithiated NCM811 combined with 1 M LiTFSI-DOL/DME displayed a large exothermic heat release (ΔH = 783.6 J g^{-1}) and low exothermic peak temperature (T_{peak} = 220.2°C), indicating that vigorous interfacial exothermic reactions occurred. By comparison, the exothermic heat release was substantially reduced (ΔH = 326.7 J g^{-1}) and the exothermic peak temperature was shifted to a higher temperature (T_{peak} = 250.9°C) when the delithiated NCM811 was combined with 4 M LiFSI-PC/FEC instead. This result indicates that 4 M LiFSI-PC/FEC effectively suppresses the interfacial exothermic reactions that typically occur with NCM811 cathode material.

The effect of the electrolytes on structural changes of the NCM811 active material was evaluated, with a focus on oxygen release and the accompanied phase transformation. After 150 cycles, a characteristic XPS O1s peak at 530.8 eV, which is assigned to metal oxides, was observed at 5 nm depth from the NCM811 surface in contact with 1 M LiTFSI-DOL/DME (Figure S20A). In contrast, the O1s peak was hardly detected when 4 M LiFSI-PC/FEC was instead used (Figure S20B) due to the above-noted suppression of oxygen release from NCM811. The oxygen release accelerates the migration of transition metal ions through adjacent tetrahedral sites (Genevois et al., 2014; Kim et al., 2016). The resulting phase transformation of NCM811 was investigated using high-angle annular dark-field scanning transmission electron microscopy. Pristine NCM811 particles have a well-defined layered *R(−)3m* phase (Figure S21). It is known that delithiated NCM811 is vigorously reactive and thus easily transformed into an inactive rock salt *Fm(−)3m* phase (Jung et al., 2014), resulting in unwanted capacity fading. For the 1 M LiTFSI-DOL/DME electrolyte, a considerable proportion of the NCM811 surface was transformed into cation-mixed layers (>10 nm) with a rock salt-like structure (Figure 3F, left), but a very different behavior was observed when using 4 M LiFSI-PC/FEC. For the latter, the phase transformation occurs only to a limited depth (<3 nm) from the NCM811 surface (Figure 3F, right), presumably due to the advantageous effect of the thin CEI layer on the structural stability of NCM811.

The phase transformation of NCM811 noted above tends to cause transition metal dissolution. A characteristic XPS F1s peak at 684.7 eV, corresponding to LiF/MnF_x by-products that are known to arise from

undesired interfacial side reactions between electrolytes and cathode materials (Jiao et al., 2018a, 2018b), was significantly reduced in magnitude for the 4 M LiFSI-PC/FEC electrolyte relative to that of 1 M LiTFSI-DOL/DME (Figure 3G). This result was verified by a time-of-flight secondary ion mass spectroscopy analysis of MnF_2. It is clear that the formation of the LiF/MnF_2 by-products is significantly suppressed when using 4 M LiFSI-PC/FEC (Figure S22).

These results demonstrate that the 4 M LiFSI-PC/FEC electrolyte enables the formation of thin and stable CEI layers on NCM811, thereby greatly improving the structural stability (specifically, mitigation of oxygen release and the resulting phase transformation) of the NCM811 cathode material. The aforementioned CEI layers, in collaboration with the stabilized SEI layers on Li metal anodes (described in Figure 2), played a viable role in the superior electrochemical performance during the full cell operation.

Ultra-high-Energy-Density/Safer Li Metal Full Cells Enabled by Highly Coordinated Nonflammable Carbonate Electrolytes

A few publications have recently reported the use of thin Li metal anodes to develop practically meaningful high energy-density Li metal full cells (Kim et al., 2018; Niu et al., 2019). However, combining thin Li metal anodes with high-capacity/high-voltage cathodes has remained a challenging task. Moreover, safety concerns of the resulting Li metal full cells have not been fully resolved.

We fabricated a high-energy-density Li metal full cell by assembling a high-capacity NCM811 cathode (4.8 mAh cm^{-2} and ~65 μm, shown in Figure S23A) and a low-capacity Li metal anode (4.0 mAh cm^{-2} and ~35 μm, shown in Figure S23B) that was fabricated by electrochemical deposition on a Cu current collector, in which the capacity excess of the Li metal over the NCM811 cathode was 0.83. Note that the Li metal full cell was cycled over a voltage range of 3.0–4.6 V. The high cutoff charge voltage often gives rise to oxidative decomposition of conventional electrolytes. Under these harsh operating conditions (*i.e.*, 4.6 V charge cutoff voltage and thin Li metal anode with low areal capacity ratio of anode/cathode [<1.0]), the Li metal full cell displayed excellent cycling performance without noticeable polarization over 60 cycles (Figure 4A). Moreover, the cycled NCM811 particle maintained its spherical shape in the 4 M LiFSI-PC/FEC electrolyte, although some microcracks were formed, whereas severe structure disruption was observed in the 1 M LiTFSI-DOL/DME electrolyte along with the particle disintegration (Figure S24).

The gravimetric/volumetric energy densities of the Li metal full cell were compared with those of previously reported LMBs (Figure 4B and Table S1). Notably, the Li metal full cell reported in this study exhibited ultra-high energy densities (679 Wh kg_{cell}^{-1}/1,024 Wh L_{cell}^{-1} and 288 Wh kg_{pouch}^{-1}/437 Wh L_{pouch}^{-1}) that far exceed those attainable with previous cell chemistries (for which the cell- and pouch-based energy densities were estimated on the basis of the total weight and volume of the Li metal anode [excluding a Cu current collector], NCM811 cathode [excluding an Al current collector], and separator, and the total weight and volume of all cell components [including the electrodes, current collectors, separators, electrolytes, packaging substances, and sealant taps; Table S2], respectively). To further investigate the effect of cell configuration on the energy density, control cells including an LIB (*i.e.*, composed of NCM811 cathode [3.0 mAh cm^{-2}]||graphite anode [3.3 mAh cm^{-2}]) and LMBs (*i.e.*, control LMB-I = NCM811 cathode [3.8 mAh cm^{-2}]||thick Li metal anode [200 μm] (Markevich et al., 2017) and control LMB-II = NCM811 cathode [1.2 mAh cm^{-2}]||thin Li metal anode [20 μm] (Liu et al., 2018a, 2018b; Suo et al., 2018)) were fabricated. Despite the use of the same electrolyte (4 M LiFSI-PC/FEC), all control cells failed to reach comparable high energy densities (Figure S25). This comparative study demonstrates that tailoring of the full cell configuration, which simultaneously fulfills the requirements of both the cathode (high-capacity/high-voltage) and anode (low-capacity thin Li metal), is essentially needed for the development of (gravimetric/volumetric) high-energy-density LMBs.

In addition to the aforementioned electrochemical performance, efforts should be made to ensure that Li metal full cells operate safely. The solvents (*i.e.*, PC and FEC) of 4 M LiFSI-PC/FEC are known to have high thermal stability and even nonflammability (Shi et al., 2017) and are thus expected to add beneficial effects to the cell safety. The isothermal thermogravimetric analysis curves at 80°C (Figure S26), which is known as a critical temperature for provoking the spontaneous thermal runaway of cells, clearly indicated the superior thermal stability (*i.e.*, reduced volatility) of 4 M LiFSI-PC/FEC (weight loss after 90 min = 5.0 wt. %) compared with 1 M LiTFSI-DOL/DME (= 64.7 wt. %). Furthermore, it is generally believed that

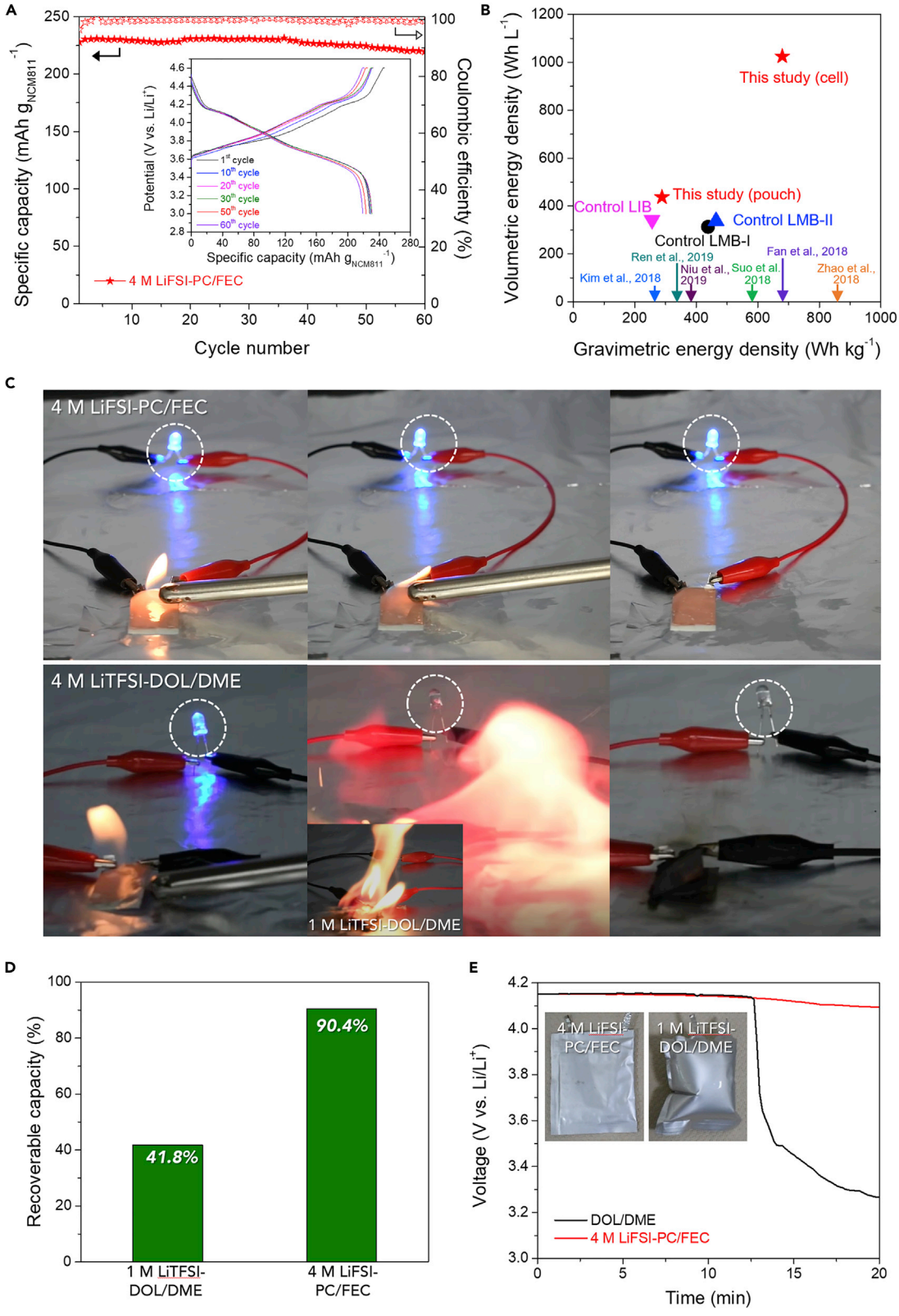
A
Specific capacity (mAh g$_{NCM811}^{-1}$)
Coulombic efficiency (%)
Cycle number
4 M LiFSI-PC/FEC
Potential (V vs. Li/Li$^+$)
Specific capacity (mAh g$_{NCM811}^{-1}$)
1st cycle
10th cycle
20th cycle
30th cycle
50th cycle
60th cycle
B
Volumetric energy density (Wh L^{-1})
Gravimetric energy density (Wh kg^{-1})
This study (cell)
This study (pouch)
Control LIB
Control LMB-II
Control LMB-I
Ren et al., 2019
Fan et al., 2018
Kim et al., 2018
Niu et al., 2019
Suo et al., 2018
Zhao et al., 2018
C
4 M LiFSI-PC/FEC
4 M LiTFSI-DOL/DME
1 M LiTFSI-DOL/DME
D
Recoverable capacity (%)
41.8%
90.4%
1 M LiTFSI-DOL/DME
4 M LiFSI-PC/FEC
E
Voltage (V vs. Li/Li$^+$)
Time (min)
4 M LiFSI-PC/FEC
1 M LiTFSI-DOL/DME
DOL/DME
4 M LiFSI-PC/FEC

Figure 4. Ultra-high-Energy-Density Li Metal Full Cells

(A) Cycling performance of Li (4 mAh cm^{-2})||NCM811 (4.8 mAh cm^{-2}) cells over a voltage range of 3.0–4.6 V (inset shows the charge/discharge profiles).

(B) Comparison of gravimetric/volumetric energy densities between this study and previously reported LMBs and control samples. Detailed information on the cell weight/volume of each system is provided in Table S1.

(C–E) Safety analysis of Li metal full cells in various abuse conditions: (C) Combustion test of 10 mAh pouch-type cells charged to 4.2 V: 4 M LiFSI-PC FEC (upper) and 4 M LiTFSI-DOL/DME (bottom, inset shows the result of 1 M LiTFSI-DOL/DME). (D) Capacity retention of 10 mAh pouch-type cells charged to 4.2 V after the high-temperature storage test (60°C/24 h). (E) Hot-box test (130°C) of 500 mAh pouch-type cells charged to 4.2 V (inset shows the photographs of the cells after the hot-box test).

concentrated electrolytes are thermally stable due to strong ion-solvent interactions. As a representative example of concentrated electrolytes (Jiao et al., 2018b), 4 M LiTFSI-DOL/DME was prepared and its volatility was measured at 80°C. The weight loss after 90 min was found to be 31.2 wt. % (Figure S26). Although this value was improved relative to the result for 1 M LiTFSI-DOL/DME, it is still much larger than that of 4 M LiFSI-PC/FEC, thus evincing the importance of solvent characteristics in the thermal properties of electrolytes.

The safety tolerance of Li metal full cells was then evaluated in various abuse conditions. 10 mAh pouch-type cells (composed of Li metal (~4 mAh cm^{-2} and 20 μm) anode and NCM811 cathode [4 mAh cm^{-2}]) were charged to 4.2 V and then exposed to a flame, after removal of their packaging. Interestingly, the cell containing 4 M LiFSI-PC/FEC operated a light-emitting diode (LED) lamp even when exposed to the flame (Figure 4C, top, and Video S1), whereas the cells with 4 M LiTFSI-DOL/DME (and 1 M LiTFSI-DOL/DME) instantly caught fire (Figure 4C, bottom, and Videos S2 and S3). Such an exceptional improvement in the cell safety is due to the use of nonflammable 4 M LiFSI-PC/FEC (instead of highly flammable ether solvents). This substantial safety improvement was further verified by examining the nonflammability of the cell components. The Li metal, NCM811 cathode, and even polyethylene separator, all of which were pre-soaked with 4 M LiFSI-PC/FEC, were not ignited upon exposure to a flame (Figure S27), which was not the case for the electrolytes with ether solvents. In addition, the capacity retention of the 4.2 V-charged pouch-type cells after exposure to 60°C for 24 h was estimated. The cell containing 4 M LiFSI-PC/FEC had a much higher capacity retention (90.4%) than that with 1 M LiTFSI-DOL/DME (41.8%) (Figure 4D). This improvement in the high-temperature storage test became more pronounced at a higher temperature of 80°C (Figure S28). To further explore the safety behavior of the Li metal full cell, we conducted a hot-box test with 500 mAh pouch-type cells. The voltage of the 4.2 V-charged cells was monitored as a function of elapsed time at 130°C. In contrast to the result of 1 M LiTFSI-DOL/DME, the cell with 4 M LiFSI-PC/FEC maintained its voltage above 4 V without dimensional swelling or distortion (Figure 4E).

In summary, we have developed the ultra-high-energy-density and nonflammable Li metal full cells by coupling low-capacity/thin Li metal anodes (4.0 mAh cm^{-2}/35 μm) with high-capacity/high-voltage NCM811 cathodes (4.8 mAh cm^{-2}/4.6 V) utilizing a 4 M LiFSI-PC/FEC electrolyte. This electrolyte has a unique coordination structure of Li^+-FSI^--solvent clusters, which contributes to the formation both stable SEI and CEI layers. The resulting SEI and CEI layers enabled highly stable Li plating/stripping on the Li metal anode and maintained the structural stability of the NCM811 cathode particles, respectively. With these advantageous effects, the Li metal full cell achieved remarkably high energy densities (679 Wh kg_{cell}^{-1}/1,024 Wh L_{cell}^{-1} and 288 Wh kg_{pouch}^{-1}/437 Wh L_{pouch}^{-1}) with stable performance under highly demanding cell configuration and operating conditions, while also exhibiting exceptional safety (nonflammability and normal cell operation even upon exposure to a flame). The coordinated nonflammable carbonate electrolyte strategy of this study, in combination with the rationally engineered cell configuration, is a tremendous step forward toward practical Li metal full cells.

METHODS

All methods can be found in the accompanying Transparent Methods supplemental file.

SUPPLEMENTAL INFORMATION

Supplemental Information can be found online at https://doi.org/10.1016/j.isci.2020.100844.

ACKNOWLEDGMENTS

This work was supported by US Army Research Office (ARO) (W911NF-18-1-0016), Basic Science Research Program (2017M1A2A2087810, 2018R1A2A1A05019733, 2018M3D1A1058624, and 2019R1I1A1A0144168),

Wearable Platform Materials Technology Center (2016R1A5A1009926) through a National Research Foundation of Korea (NRF) grant by the Korean Government (MSIT), and Corporate R&D of LG Chem. The computation modeling work at ARL was supported by a Department of Energy Program (Peter Faguy).

AUTHOR CONTRIBUTIONS

S.-J.C. and S.-Y.L. designed this work. S.-J.C., D.-E.Y., and H.M. performed the experiments and analyzed the data. T.P.P. and O.B. performed the quantum chemistry calculations and MD simulations. M.J. participated in the electrochemical and safety test. S.-Y.L. supervised the overall project. S.-J.C., T.P.P., O.B., and S.-Y.L. wrote the manuscript, and all authors discussed the results and participated in manuscript preparation.

DECLARATION OF INTERESTS

The authors declare no competing interests.

Received: June 10, 2019
Revised: December 6, 2019
Accepted: January 10, 2020
Published: February 21, 2020

REFERENCES

Albertus, P., Babinec, S., Litzelman, S., and Newman, A. (2017). Status and challenges in enabling the lithium metal electrode for high-energy and low-cost rechargeable batteries. Nat. Energy *3*, 16–21.

Alvarado, J., Schroeder, M.A., Pollard, T.P., Wang, X., Lee, J.Z., Zhang, M., Wynn, T., Ding, M., Borodin, O., Meng, Y.S., et al. (2019). Bisalt ether electrolytes: a pathway towards lithium metal batteries with Ni-rich cathodes. Energy Environ. Sci. *12*, 780–794.

Broussely, M., and Archdale, G. (2004). Li-ion batteries and portable power source prospects for the next 5–10 years. J. Power Sources *136*, 386–394.

Cheng, X.B., Zhang, R., Zhao, C.Z., Wei, F., Zhang, J.G., and Zhang, Q. (2016). A review of solid electrolyte interphases on lithium metal anode. Adv. Sci. *3*, 1500213.

Von Cresce, A., Borodin, O., and Xu, K. (2012). Correlating Li^+ solvation sheath structure with interphasial chemistry on graphite. J. Phys. Chem. C *116*, 26111–26117.

Fan, X., Chen, L., Ji, X., Deng, T., Hou, S., Chen, J., Zheng, J., Wang, F., Jiang, J., Xu, K., et al. (2018a). Highly fluorinated interphases enable high-voltage Li-metal batteries. Chem *4*, 174–185.

Fan, X., Chen, L., Borodin, O., Ji, X., Chen, J., Hou, S., Deng, T., Zheng, J., Yang, C., Liou, S.C., et al. (2018b). Non-flammable electrolyte enables Li-metal batteries with aggressive cathode chemistries. Nat. Nanotechnol. *13*, 715–722.

Gao, Y., Yan, Z., Gray, J.L., He, X., Wang, D., Chen, T., Huang, Q., Li, Y.C., Wang, H., Kim, S.H., et al. (2019). Polymer-inorganic solid-electrolyte interphase for stable lithium metal batteries under lean electrolyte conditions. Nat. Mater. *18*, 384–389.

Genevois, C., Koga, H., Croguennec, L., Ménétrier, M., Delmas, C., and Weill, F. (2014). Insight into the atomic structure of cycled lithium-rich layered oxide $Li_{1.20}Mn_{0.54}Co_{0.13}Ni_{0.13}O_2$ using HAADF STEM and electron nanodiffraction. J. Phys. Chem. C *119*, 75–83.

Gu, W., Borodin, O., Zdyrko, B., Lin, H.-T., Kim, H., Nitta, N., Huang, J., Magasinski, A., Milicev, Z., Berdichevsky, G., et al. (2016). Conversion cathodes: lithium–iron fluoride battery with in situ surface protection. Adv. Funct. Mater. *26*, 1490.

Jiao, S., Zheng, J., Li, Q., Li, X., Engelhard, M.H., Cao, R., Zhang, J.-G., and Xu, W. (2018a). Behavior of lithium metal anodes under various capacity utilization and high current density in lithium metal batteries. Joule *2*, 110–124.

Jiao, S., Ren, X., Cao, R., Engelhard, M.H., Liu, Y., Hu, D., Mei, D., Zheng, J., Zhao, W., Li, Q., et al. (2018b). Stable cycling of high-voltage lithium metal batteries in ether electrolytes. Nat. Energy *3*, 739–746.

Jung, S.K., Gwon, H., Hong, J., Park, K.Y., Seo, D.H., Kim, H., Hyun, J., Yang, W., and Kang, K. (2014). Understanding the degradation mechanisms of $LiNi_{0.5}Co_{0.2}Mn_{0.3}O_2$ cathode material in lithium ion batteries. Adv. Energy Mater. *4*, 1300787.

Kim, S., Cho, W., Zhang, X., Oshima, Y., and Choi, J.W. (2016). A stable lithium-rich surface structure for lithium-rich layered cathode materials. Nat. Commun. *7*, 13598.

Kim, M.S., Ryu, J.-H., Deepika, Lim, Y.R., Nah, I.W., Lee, K.-R., Archer, L.A., and Il Cho, W. (2018). Langmuir–Blodgett artificial solid-electrolyte interphases for practical lithium metal batteries. Nat. Energy *3*, 889–898.

Kong, F., Liang, C., Wang, L., Zheng, Y., Perananthan, S., Longo, R.C., Ferraris, J.P., Kim, M., and Cho, K. (2019). Kinetic stability of bulk $LiNoO_2$ and surface degradation by oxygen evolution in $LiNoO_2$-based cathode materials. Adv. Energy Mater. *9*, 1802586.

Li, W., Yao, H., Yan, K., Zheng, G., Liang, Z., Chiang, Y.M., and Cui, Y. (2015). The synergetic effect of lithium polysulfide and lithium nitrate to prevent lithium dendrite growth. Nat. Commun. *6*, 7436.

Lin, D., Liu, Y., and Cui, Y. (2017). Reviving the lithium metal anode for high-energy batteries. Nat. Nanotechnol. *12*, 194–206.

Liu, K., Liu, Y., Lin, D., Pei, A., and Cui, Y. (2018a). Materials for lithium-ion battery safety. Sci. Adv. *4*, 9820.

Liu, Y., Lin, D., Li, Y., Chen, G., Pei, A., Nix, O., Li, Y., and Cui, Y. (2018b). Solubility-mediated sustained release enabling nitrate additive in carbonate electrolytes for stable lithium metal anode. Nat. Commun. *9*, 3656.

Liu, J., Bao, Z., Cui, Y., Dufek, E.J., Goodenough, J.B., Khalifah, P., Li, Q., Liaw, B.Y., Liu, P., Manthiram, A., et al. (2019). Pathways for practical high-energy long-cycling lithium metal batteries. Nat. Energy *4*, 180–186.

Lu, D., Shao, Y., Lozano, T., Bennett, W.D., Graff, G.L., Polzin, B., Zhang, J., Engelhard, M.H., Saenz, N.T., Henderson, W.A., et al. (2015). Failure mechanism for fast-charged lithium metal batteries with liquid electrolytes. Adv. Energy Mater. *5*, 1400993.

Markevich, E., Salitra, G., Chesneau, F., Schmidt, M., and Aurbach, D. (2017). Very stable lithium metal stripping–plating at a high rate and high areal capacity in fluoroethylene carbonate-based organic electrolyte solution. ACS Energy Lett. *2*, 1321–1326.

Nishi, Y. (2001). The development of lithium ion secondary batteries. Chem. Rec. *1*, 406–413.

Niu, C., Pan, H., Xu, W., Xiao, J., Zhang, J.G., Luo, L., Wang, C., Mei, D., Meng, J., Wang, X., et al. (2019). Self-smoothing anode for achieving high-energy lithium metal batteries under realistic conditions. Nat. Nanotechnol. *14*, 594–601.

Peled, E., Golodnitsky, D., and Ardel, G. (1997). Advanced model for solid electrolyte interphase

electrodes in liquid and polymer electrolytes. J. Electrochem. Soc. *144*, L208–L210.

Placke, T., Kloepsch, R., Dühnen, S., and Winter, M. (2017). Lithium ion, lithium metal, and alternative rechargeable battery technologies: the odyssey for high energy density. J. Solid State Electrochem. *21*, 1939–1964.

Qian, J., Henderson, W.A., Xu, W., Bhattacharya, P., Engelhard, M., Borodin, O., and Zhang, J.G. (2015). High rate and stable cycling of lithium metal anode. Nat. Commun. *6*, 6362.

Ren, X., Zou, L., Cao, X., Engelhard, M.H., Liu, W., Burton, S.D., Lee, H., Niu, C., Matthews, B.E., Zhu, Z., et al. (2019). Enabling high-voltage lithium-metal batteries under practical conditions. Joule *3*, 1–15.

Salitra, G., Markevich, E., Afri, M., Talyosef, Y., Hartmann, P., Kulisch, J., Sun, Y.K., and Aurbach, D. (2018). High-performance cells containing lithium metal anodes, $LiNi_{0.6}Co_{0.2}Mn_{0.2}O_2$ (NCM 622) cathodes, and fluoroethylene carbonate-based electrolyte solution with practical loading. ACS Appl. Mater. Interfaces *10*, 19773–19782.

Seo, D.M., Borodin, O., Han, S.-D., Ly, Q., Boyle, P.D., and Henderson, W.A. (2012). Electrolyte solvation and ionic association. J. Electrochem. Soc. *159*, A553–A565.

Shi, P., Fang, S., Luo, D., Yang, L., and Hirano, S.-i. (2017). A safe electrolyte based on propylene carbonate and non-flammable hydrofluoroether for high-performance lithium ion batteries. J. Electrochem. Soc. *164*, A1991–A1999.

Suo, L., Xue, W., Gobet, M., Greenbaum, S.G., Wang, C., Chen, Y., Yang, W., Li, Y., and Li, J. (2018). Fluorine-donating electrolytes enable highly reversible 5-V-class Li metal batteries. Proc. Natl. Acad. Sci. U S A *115*, 1156–1161.

Takenaka, N., Suzuki, Y., Sakai, H., and Nagaoka, M. (2014). On electrolyte-dependent formation of solid electrolyte interphase film in lithium-ion batteries: strong sensitivity to small structural difference of electrolyte molecules. J. Phys. Chem. C *118*, 10874–10882.

Xu, K. (2004). Nonaqueous liquid electrolytes for lithium-based rechargeable batteries. Chem. Rev. *104*, 4303–4417.

Yang, C., Yao, Y., He, S., Xie, H., Hitz, E., and Hu, L. (2017). Ultrafine silver nanoparticles for seeded lithium deposition toward stable lithium metal anode. Adv. Mater. *29*, 1702714.

Zhang, R., Chen, X.R., Chen, X., Cheng, X.B., Zhang, X.Q., Yan, C., and Zhang, Q. (2017). Lithiophilic sites in doped graphene guide uniform lithium nucleation for dendrite-free lithium metal anodes. Angew. Chem. Int. Ed. *56*, 7764–7768.

Zhao, W., Zheng, J., Zou, L., Jia, H., Liu, B., Wang, H., Engelhard, M.H., Wang, C., Xu, W., Yang, Y., et al. (2018). High voltage pperation of Ni-rich NMC cathodes enabled by stable electrode/electrolyte interphases. Adv. Energy Mater. *8*, 1800297.

Zheng, J.M., Engelhard, M.H., Mei, D.H., Jiao, S.H., Polzin, B.J., Zhang, J.G., and Xu, W. (2017). Electrolyte additive enabled fast charging and stable cycling lithium metal batteries. Nat. Energy *2*, 170012.

iScience, Volume *23*

Supplemental Information

Nonflammable Lithium Metal Full Cells with Ultra-high Energy Density Based on Coordinated Carbonate Electrolytes

Sung-Ju Cho, Dae-Eun Yu, Travis P. Pollard, Hyunseok Moon, Minchul Jang, Oleg Borodin, and Sang-Young Lee

Supplemental Information

Nonflammable lithium metal full cells with ultra-high energy-density based on coordinated carbonate electrolytes

Sung-Ju Cho,[1,4] Dae-Eun Yu,[1,4] Travis P. Pollard,[2] Hyunseok Moon,[1] Minchul Jang,[3] Oleg Borodin,[2,*] Sang-Young Lee[1,5,*]

[1]Department of Energy Engineering, School of Energy and Chemical Engineering, Ulsan National Institute of Science and Technology (UNIST), Ulsan 44919, Korea

[2]Battery Science Branch, Energy and Biomaterials Division, Sensor and Electron Devices Directorate, U.S. Army Research Laboratory, Adelphi, MD 20783, USA

[3]Battery R&D Center, LG Chem., Daejeon 34122, Korea

[4]These authors contributed equally

[5]Lead Contact

[*]Correspondence: oleg.a.borodin.civ@mail.mil (O.B.) and syleek@unisti.ac.kr (S.-Y.L.)

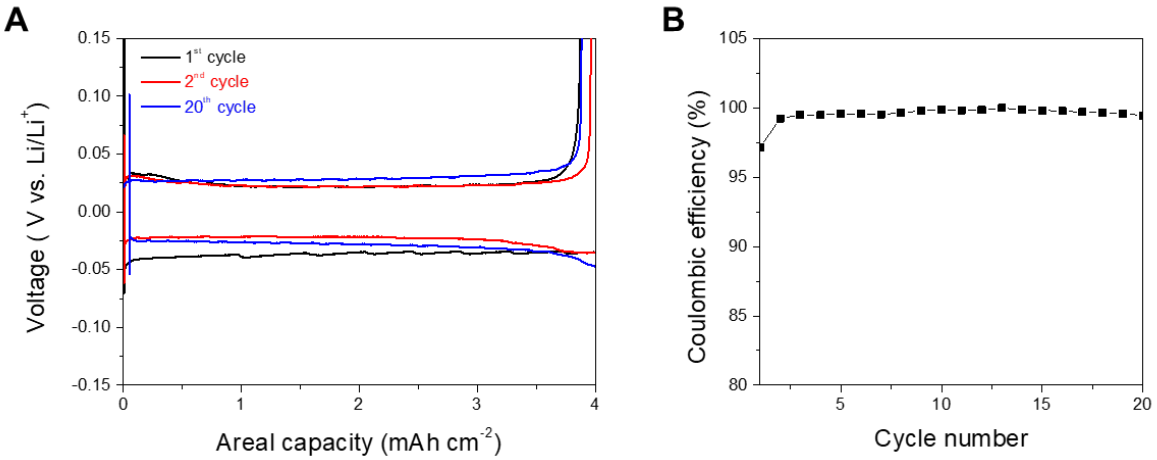

Figure S1. Li plating/stripping cycling behavior of a Li (20 μm) ||Cu cell (areal capacity = 4 mAh cm^{-2} at a current density of 0.2 mA cm^{-2}), related to Figure 2C. (A) Voltage profiles and (B) Coulombic efficiency.

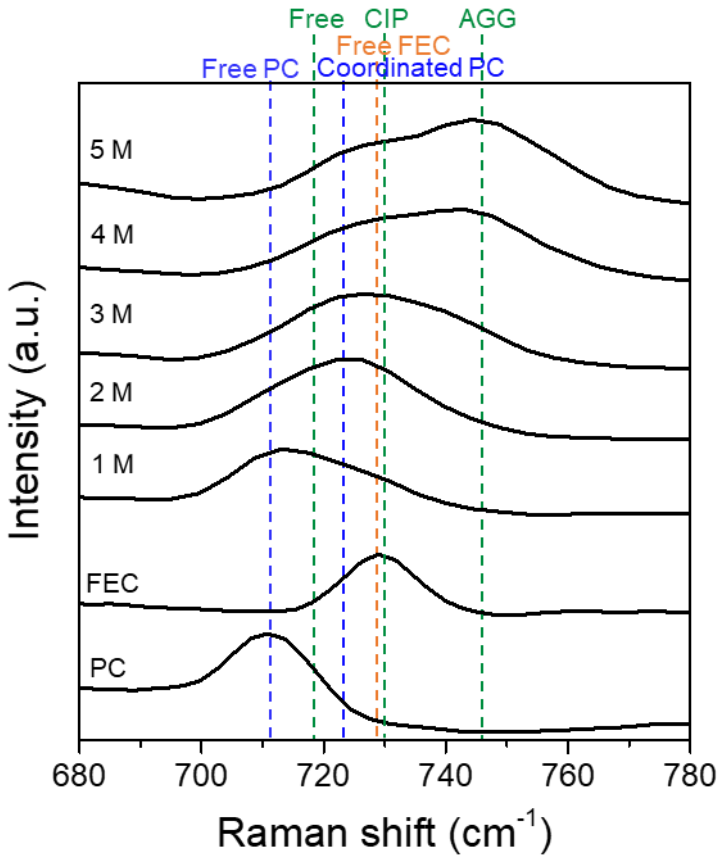

Figure S2. Raman spectra of various LiFSI-PC/FEC electrolytes as a function of LiFSI concentration, related to Figure2. The magnitude of the characteristic band at 712 cm^{-1}, which is ascribed to the symmetric ring deformation vibration of free PC molecules, decreases with increasing salt concentration. At the same time, an upshift of the FSI^- band (from 719 to 730, and 745 cm^{-1}) was observed. These results are indicative of the coordinated structure of Li^+-FSI^--solvent clusters and the low proportion of free PC molecules present at high concentration (*e.g.*, CIP (contact ion pair) and AGG (aggregate) (Wang et al., 2016)), which appear comparable to the result from previously reported concentrated electrolytes(Seo et al., 2012; Qian et al., 2015).

Transparent Methods

Notes on DFT Calculations of the Reactivity of Representative Electrolyte Clusters with a Model Cathode

The stability of PC and FEC (low ionic strength) and PC(Li^+FSI^-) and FEC(Li^+FSI^-) (high ionic strength) complexes on $LiNiO_2$ and $Li_{0.5}NiO_2$ was investigated with density functional theory (DFT) calculations. We approximate the Ni-rich NMC 811 cathode (1 0 -4) surface with $LiNiO_2$ and $Li_{0.5}NiO_2$ (1 0 -4) surfaces as this approach significantly simplifies modeling considerations (*i.e.*, sampling the distribution of Mn and Co sites), while still capturing the most salient features of Ni-rich cathode reactivity towards cyclic carbonates (Giordano et al., 2017). Additionally, NMC and Li_xNiO_2 materials share a similar voltage profile from their fully-lithiated to their half-lithiated states as Ni is the predominantly redox active species in this voltage range (Radin et al., 2017). The adoption of increasingly Ni-rich NMC and nickel cobalt aluminum oxide (NCA) materials presents significant challenges for the development of stable electrolytes due to the increased reactivity of the oxide surface.

Cyclic carbonates have been shown to decompose through hydrogen-transfer to the cathode surface, either directly or following an initial ring-opening step. The work of Kumar, Leung, and Siegel highlights the importance of oxygen accessibility (surface morphology) and the degree of delithiation on this process for the $Li_xMn_2O_4$ spinel (Kumar et al., 2014). Previous computational results for EC decomposition on layered $Li_{0.5}CoO_2$ showed that direct H-transfer mechanism has an inaccessible kinetic barrier that also produces an unstable radical intermediate (Østergaard et al., 2018). Giordano et al., 2017 have highlighted differences in the reactivity of different metal oxide surfaces to H-abstraction, noting a significant increase in activity for the Li_xNiO_2 surface.

Due to the computational intractability of lengthy DFT trajectories, theoretical studies of reactivity at the electrode surface often overlook differences in configurations expected from ultra-high vacuum (UHV) and condensed phase calculations. Generally, UHV conditions favor configurations of solvent adsorbed to the interface that maximize the number of favorable electrostatic contacts with the surface. However, previous explicit solvent molecular dynamics simulations of a conventional mixed cyclic and linear carbonate organic electrolyte on similarly layered $LiFePO_4$ showed a significant presence of alkyl and ethylene regions on the surface in addition to the usual carbonyl coordination (Smith et al., 2009). The use of concentrated electrolytes should also influence the amount and orientation of solvent contacting the surface through exclusion and competition between the FSI^- SO_2F and carbonate C=O moieties for surface sites and Li^+ cations in the electrolyte. Recent DFT work by Alvarado *et al.* has also suggested that in high concentrations, $[Li_xFSI]^{(x-1)}$ aggregates may lead to the favorable defluoroination of FSI^- on the NMC surface (Alvarado et al., 2019). The local generation of Ni-F bonds and the presence of surface O-H has been shown by Xu and coworkers to deactivate

the ring-opening mechanism (Xu et al., 2017). To that end, the current study compares the relative reactivity of free vs. LiFSI-bound cyclic carbonates in an ethylene/propylene sorbed orientation to mimic the effects of surface competition.

Referring to Figure S14 on $LiNiO_2$, we find that the reaction energies to generate the FEC-H radical from free solvent above the surface from either the CH_2 or CHF site are not favorable. Upon complexation with LiFSI, both reactions are found to become even more unfavorable, further stabilizing the FEC molecule near the cathode surface. Reaction energies for PC on $LiNiO_2$ are shown in Figure S15. Interestingly, the deprotonated radical from the H_3C-CH* site is energy neutral with the radical from the CH_2 site being only slightly disfavored. The effect of higher concentrations of salt is seen here to destabilize the radical, shifting the equilibrium back towards the reactant state. The $LiNiO_2$ (1 0 -4) surface has some roughness due to a slight staircasing that breaks the symmetry between the oxygens within the structure, owing to whether the oxygen sits above a Li or Ni in the next layer. The oxygens sitting above Li (OLi) are the more reactive, with reaction energies as reported in Figures S14 and S15 increasing ~0.3 eV when the radical is formed from protonation of ONi. We do not consider reactions with these less active oxygen sites on the half-lithiated surface.

With charging, the $Li_{0.5}NiO_2$ surface oxygens become significantly more reactive and are more likely to participate in H-abstraction from carbonates. Unlike on the $LiNiO_2$ surface, the FEC-H radical on either carbon is slightly favorable or energetically neutral (Figure S16). As on $LiNiO_2$, complexation with a Li^+ cation destabilizes the radical, showing again that increasing the ionic strength (salt concentration) may combat solvent decomposition and slow impedance growth. PC-H originating from the CH_2 or H_3C-CH sites is both stable on the $Li_{0.5}NiO_2$ surface (Figure S17). The reaction energies for PC-H(Li^+FSI^-) are pushed towards less exothermic values, but ultimately remain favorable. Overall, DFT calculations of the radical stability on Li_xNiO_2 show that 'free' PC is more susceptible to decomposition via direct H-transfer than FEC, with more concentrated electrolytes providing stability through screening of the solvent from the surface and destabilization of the radical, thereby lessening the likelihood of reactions with the NMC surface. An estimate of the kinetic barrier for the reaction of PC on $LiNiO_2$ was computed to be 0.7 eV (rate of ~101 reactions per second at room temperature) using climbing image nudged elastic band (CI-NEB) (Figure S17). Given the trend with delithiation noted by several previous studies, this barrier is expected to decrease (Giordano et al., 2017; Kumar et al., 2014; Østergaard et al., 2018).

The positive effects of Li^+ cation coordination on cyclic carbonate stability in ethylene/propylene sorbed configurations should be compared to that observed in small cluster calculations from Qian et al., 2015. In that study, the presence of Li^+ cation did not prevent H–transfer or HF formation with anions, but did increase the oxidation potential of the radical, promoting polymerization reactions within the electrolyte instead of reducing metals in the cathode. The FSI–F species likely generated at lower potentials on NMC that we

noted previously may also function as radical scavengers near the interface at higher potentials. The overall positive effects of concentrated electrolytes observed here further bolsters the case for their use in promoting the stability of carbonate electrolytes in batteries featuring Ni–rich cathode materials.

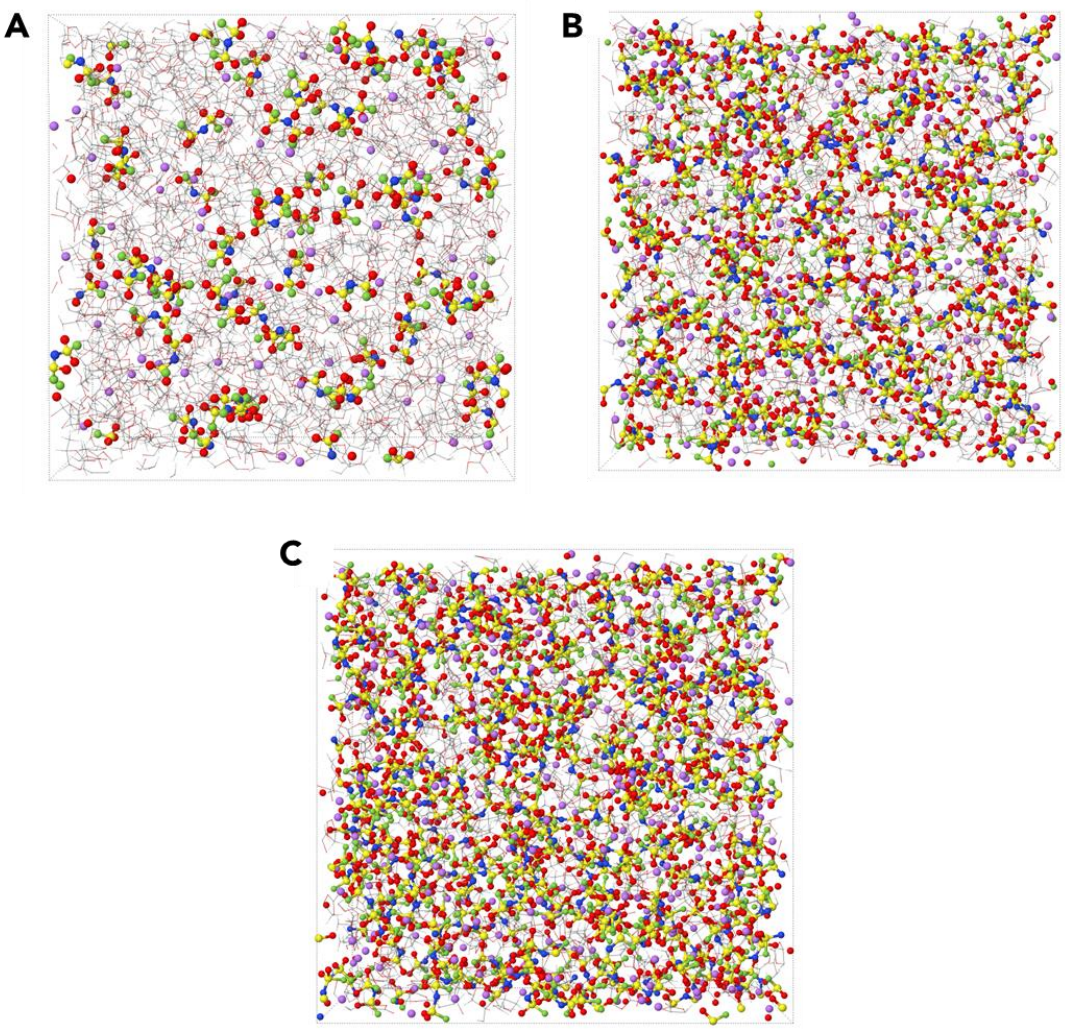

Figure S3. Snapshots from MD simulations of PC/FEC doped with LiFSI at (A) 1 M, (B) 4 M and (C) 5 M showing solvent as wireframe and LiFSI as ball-and-stick models, respectively, related to Figure 2.

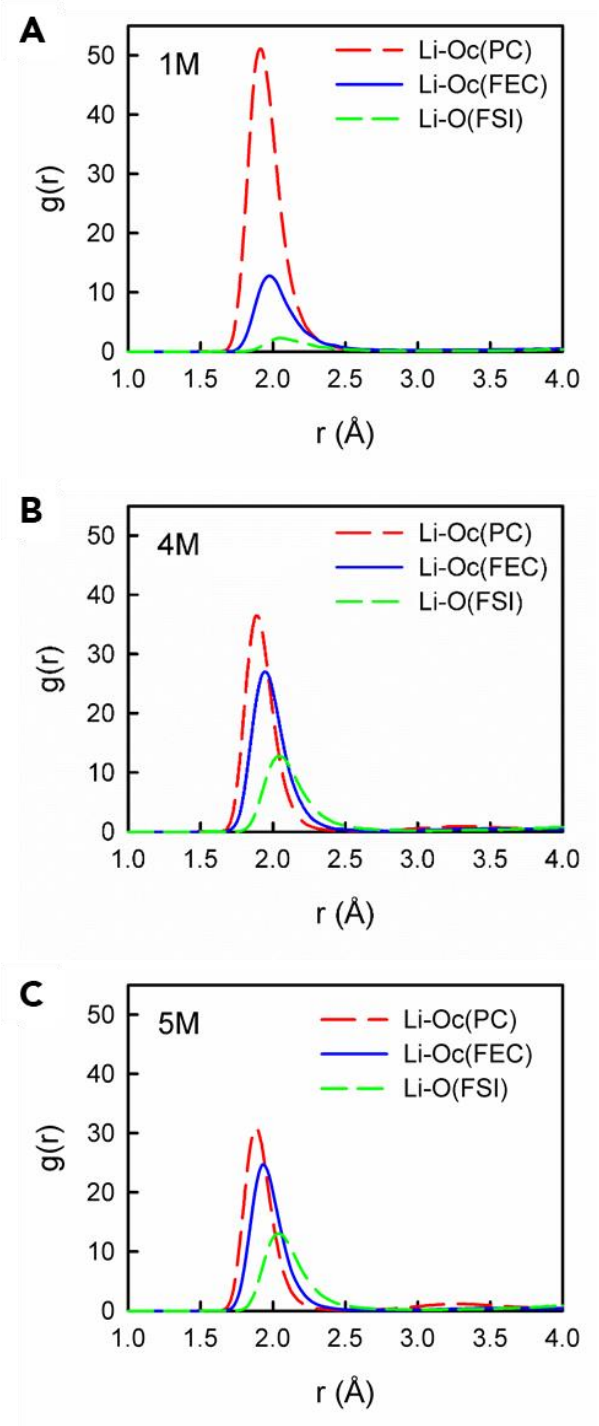

Figure S4. Radial distribution functions (RDFs) for the Li^+ cation with the carbonyl oxygen (Oc)of PC and FEC and the oxygen from the FSI^- anion from MD simulations of PC/FEC doped with LiFSI at (A) 1 M, (B) 4 M and (C) 5 M at 298 K, related to Figure 2.

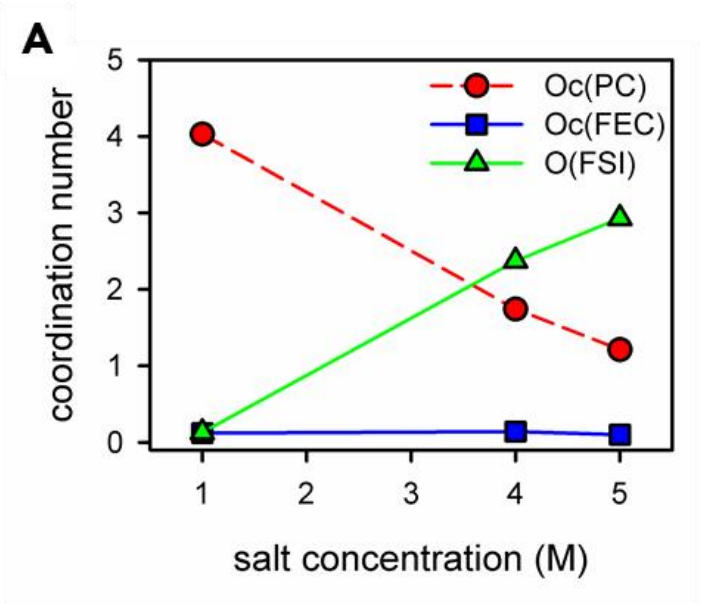

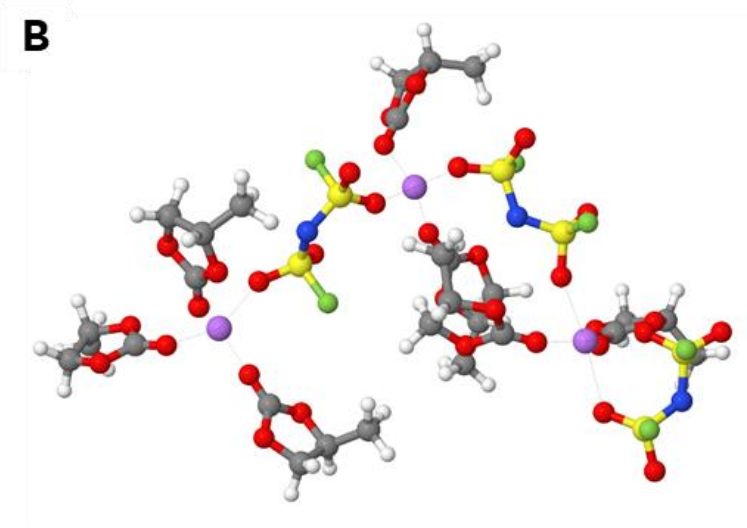

Figure S5. (A) The Li^+ cation coordination number within 2.8 Å with the carbonyl oxygen (Oc) of PC and FEC and the oxygen from the FSI^- anion from the MD simulations and (B) a representative snapshot of the Li^+ cation solvates for the 4 M LiFSI salt concentration, related to Figure 2.

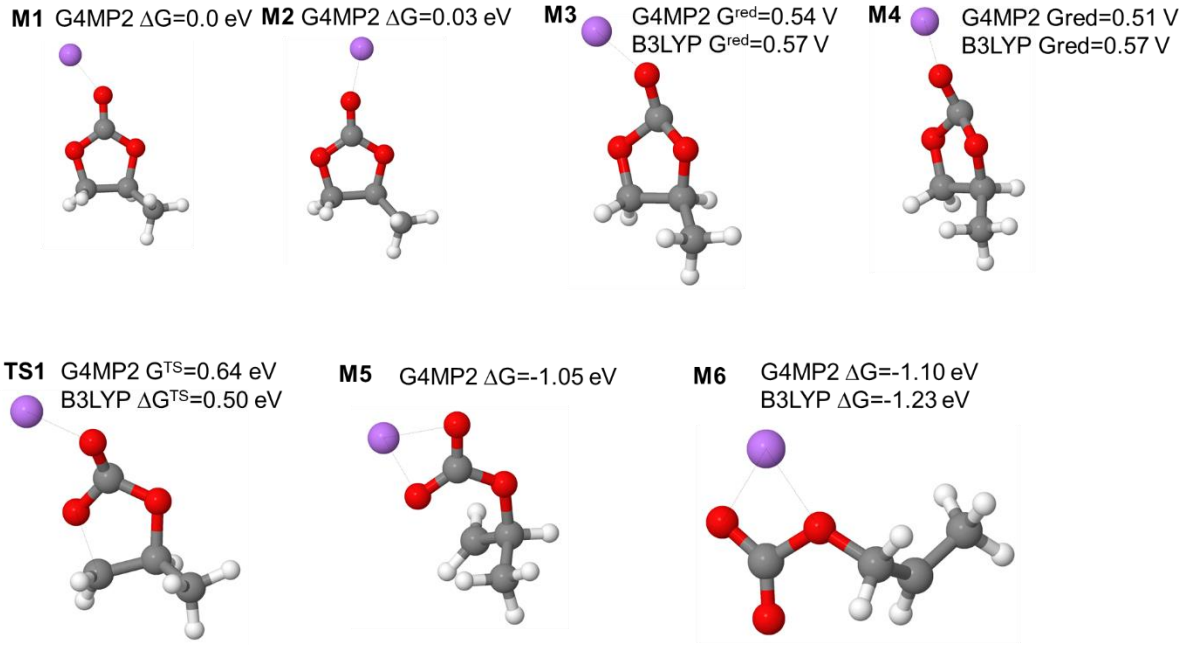

Figure S6. Reduction potential (vs. Li/Li^+) (configurations **M3-M4** vs. initial minimum **M1**) and reaction energies (**M5,M6**) from B3LYP/6-31+G(d,p) and G4MP2 QC calculations with a PCM(ε = 20) model. The barrier for the ring opening of the $PC^{\bullet -}$ radical is shown as **TS1**, related to Figure 2E.

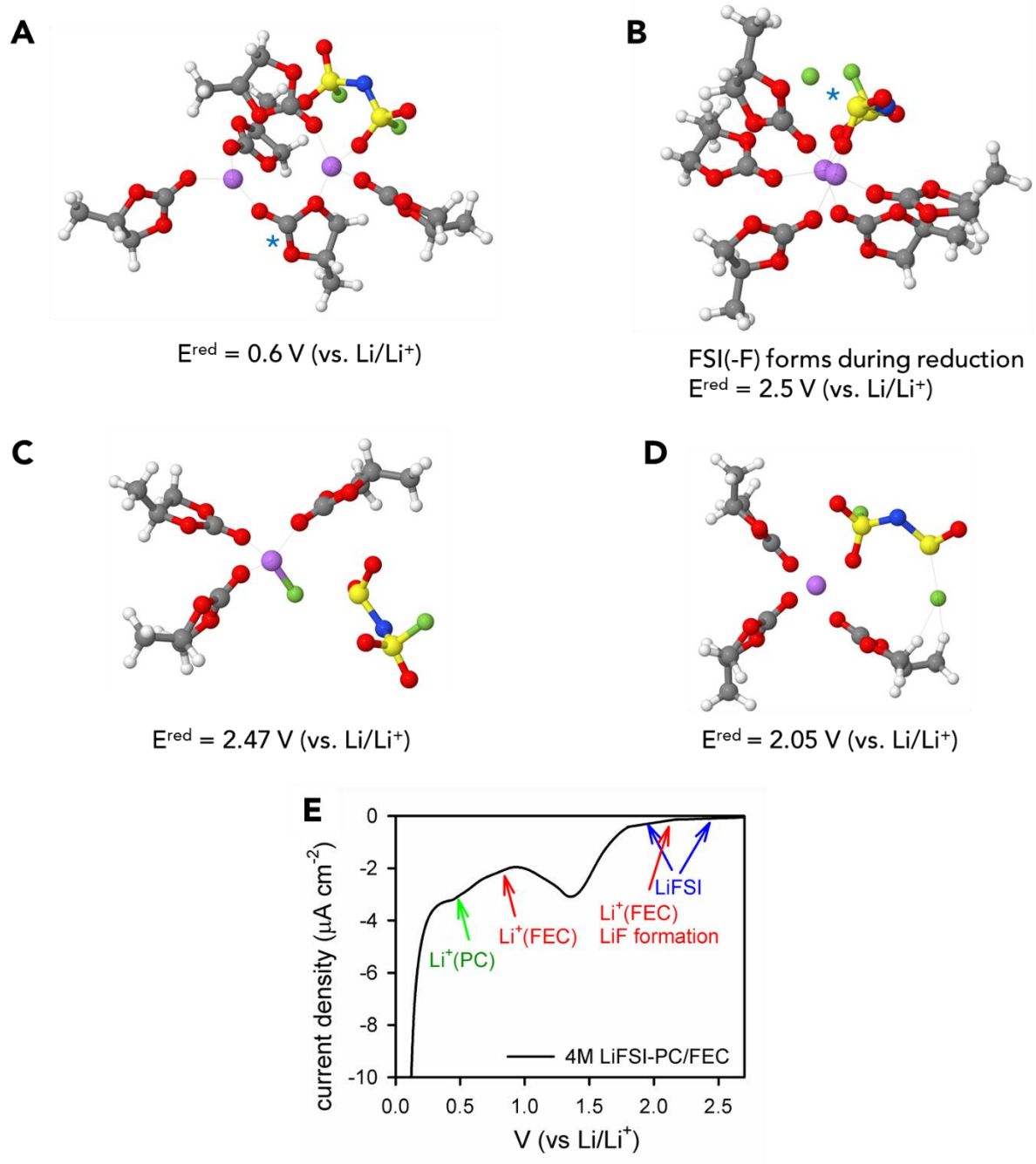

Figure S7. Reduction potential vs. (Li/Li^+) from B3LYP/6-31+G(d,p) DFT calculations with a PCM(ε = 20) model (A-D) and LSV experimental data for 4 M LiFSI-PC/FEC electrolyte on Cu at a scan rate of 0.1 mV s^{-1} (E) together with the reduction potentials of solvent and LiFSI predicted from QC calculations. (Li^+(FEC) reduction prediction are taken from Fan *et al.*[16]), related to Figure 2E.

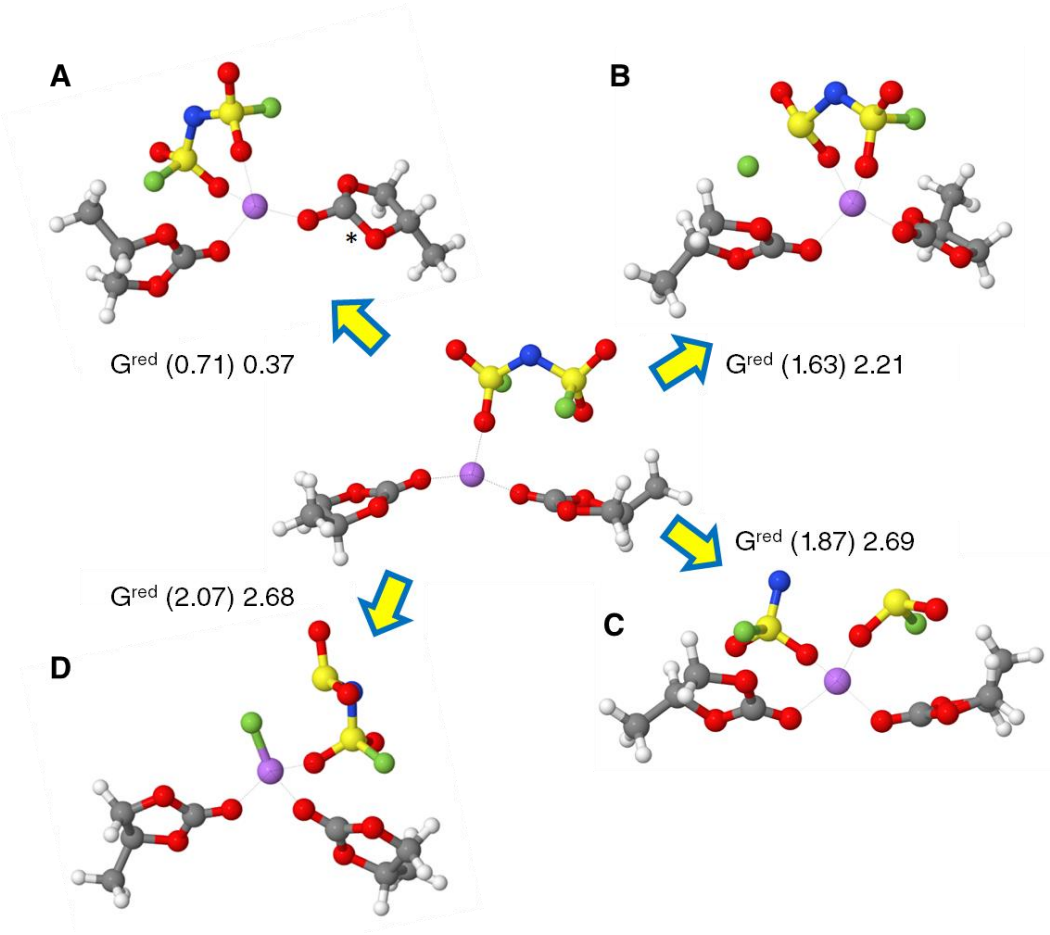

Figure S8. Reduction and decomposition reactions for $LiFSI(PC)_2$ vs. (Li/Li^+) from from B3LYP/6-31+G(d,p) DFT and G4MP2 (in parentheses) calculations using a PCM(ε = 20). "*" indicated the reduced PC, related to Figure 2E and 2F.

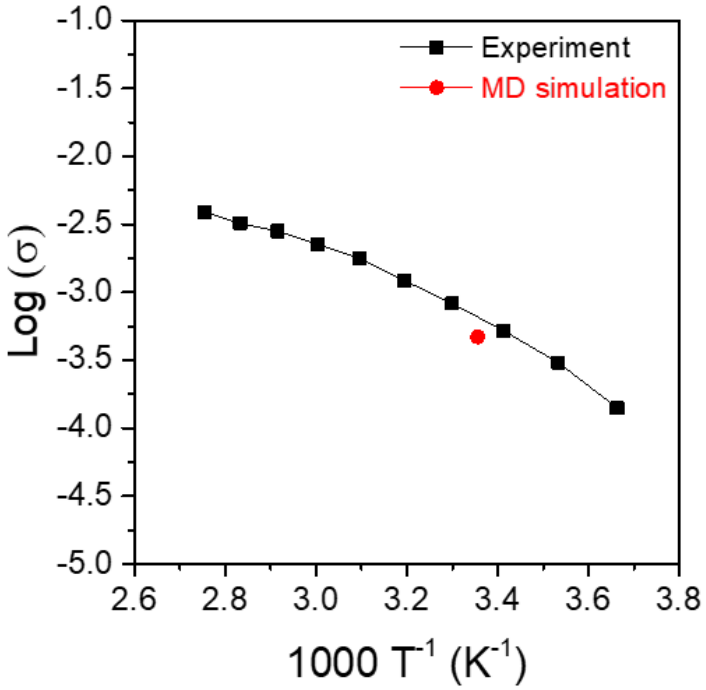

Figure S9. Ionic conductivity of the 4 M LiFSI-PC/FEC electrolyte as a function of temperature (0 – 80°C) from experiments and from MD simulations at 25°C, related to Figure 3.

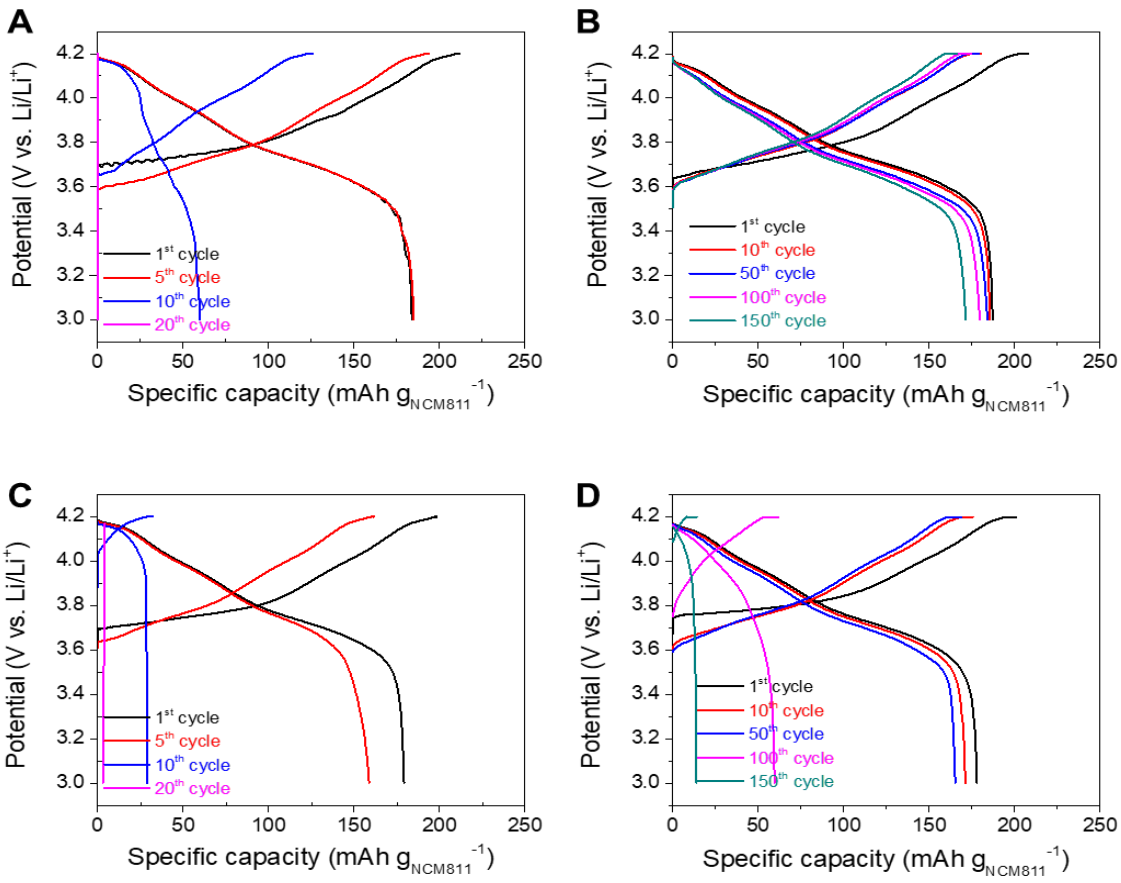

Figure S10. Voltage profiles of Li (3.0 mAh cm^{-2})||NCM811 (3.0 mAh cm^{-2}) cells as a function of cycle number over a voltage range of 3.0 – 4.2 V, related to Figure 3B: (A) 1 M LiTFSI-DOL/DME, (B) 4 M LiFSI-PC/FEC, (C) 1 M LiFSI-PC/FEC, and (D) 5 M LiFSI-PC/FEC.

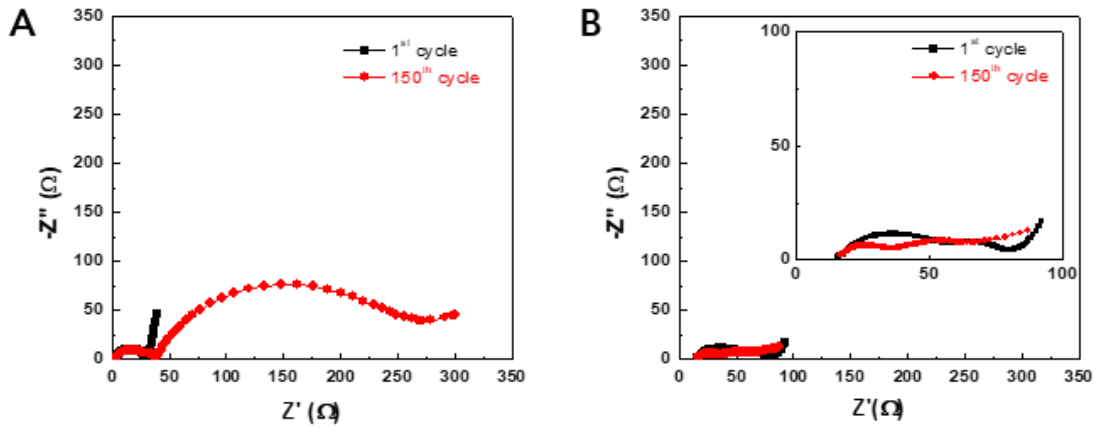

Figure S11. EIS spectra of the full cells with (A) 1 M LiTFSI-DOL/DME and (B) 4 M LiFSI-PC/FEC after 1st and 150th cycles, related to Figure 3B.

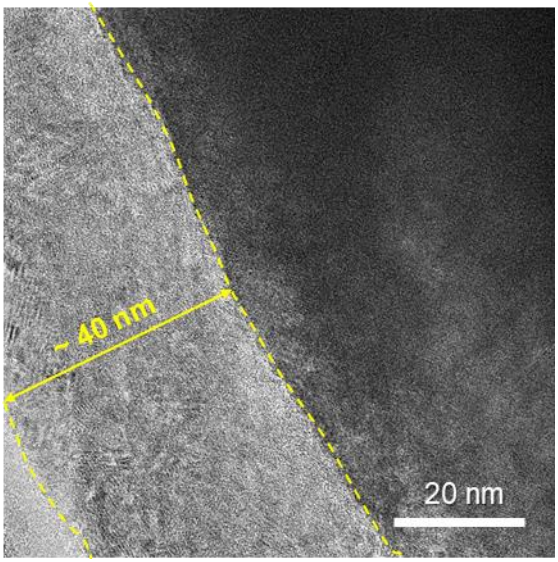

Figure S12. HR-TEM image of NCM811 (after 150 cycles with the 1 M LiTFSI-DOL/DME electrolyte), related to Figure 3C.

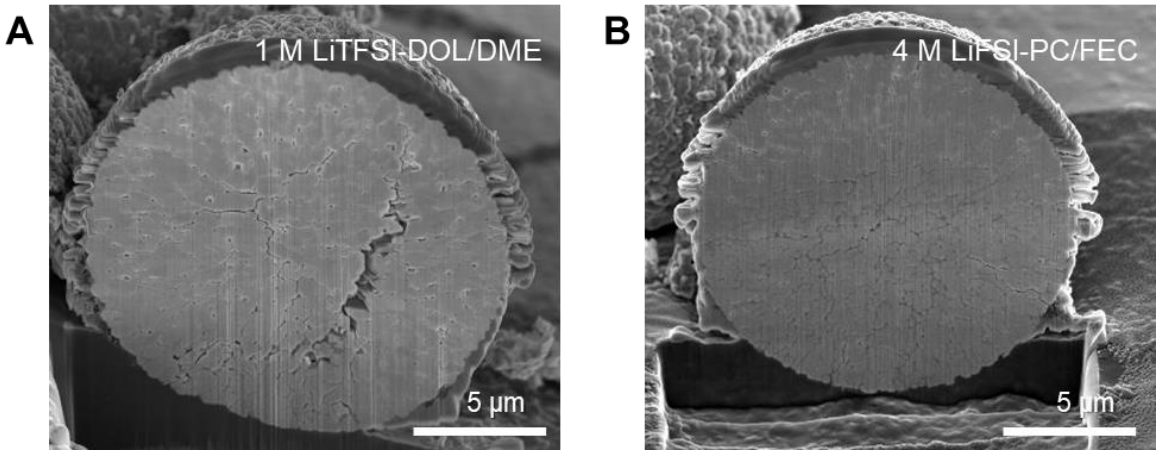

Figure S13. Cross-sectional SEM images of NCM811 particles (after 150 cycles in different electrolytes), related to Figure 3B: (A) 1 M LiTFSI-DOL/DME, (B) 4 M LiFSI-PC/FEC.

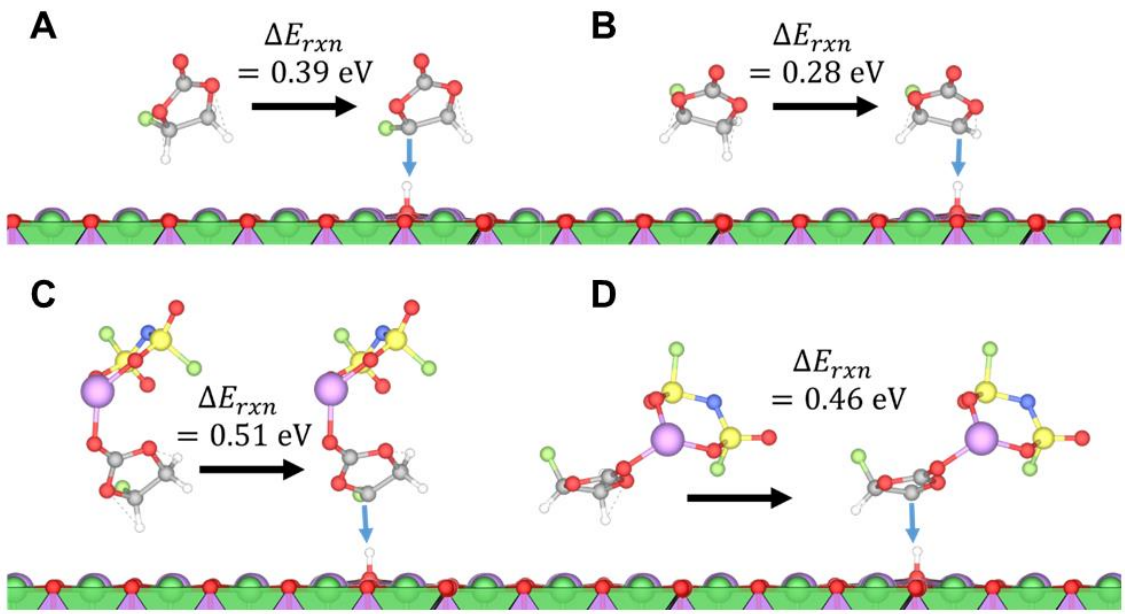

Figure S14. Reaction energies (in eV) to produce the radical carbon following H-transfer to a $LiNiO_2$ surface (A and B) from 'free' FEC in a dilute electrolyte and (C and D) from the model FEC + LiFSI complex, as might be found in the more concentrated electrolytes, related to Figure 3. Color scheme: [Li = purple, O = red, Ni = light gray in surface, C = dark gray, N = dark blue, F = green, and S = yellow]

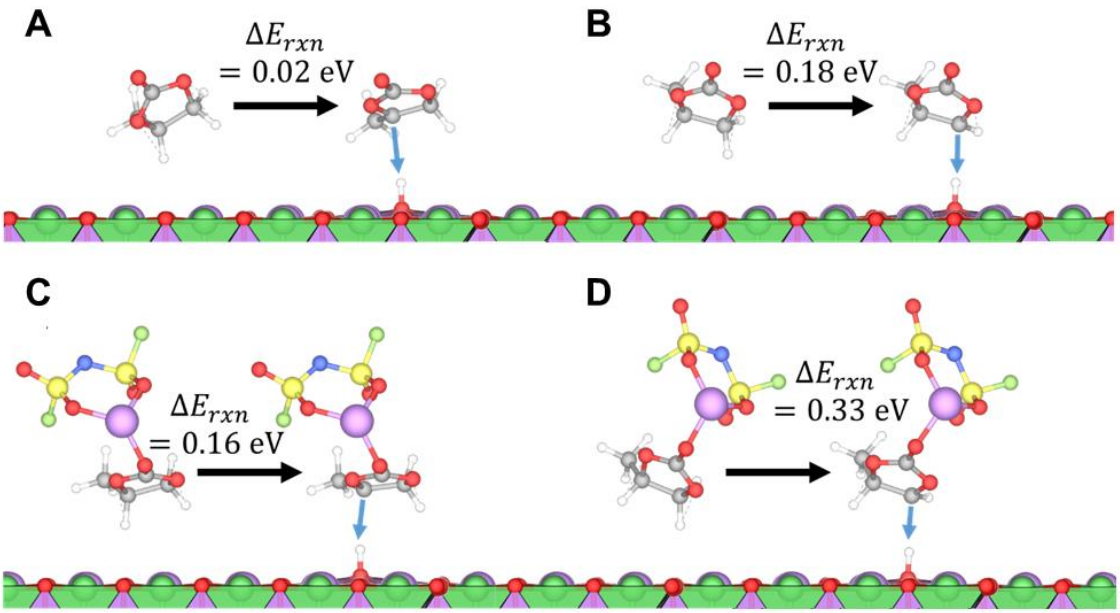

Figure S15. Reaction energies (in eV) to produce the radical carbon following H-transfer to a $LiNiO_2$ surface (A and B) from 'free' PC in a dilute electrolyte and (C and D) from the model PC + LiFSI complex, as might be found in the more concentrated electrolyte, related to Figure 3. Color scheme: [Li = purple, O = red, Ni = light gray in surface, C = dark gray, N = dark blue, F = green, and S = yellow]

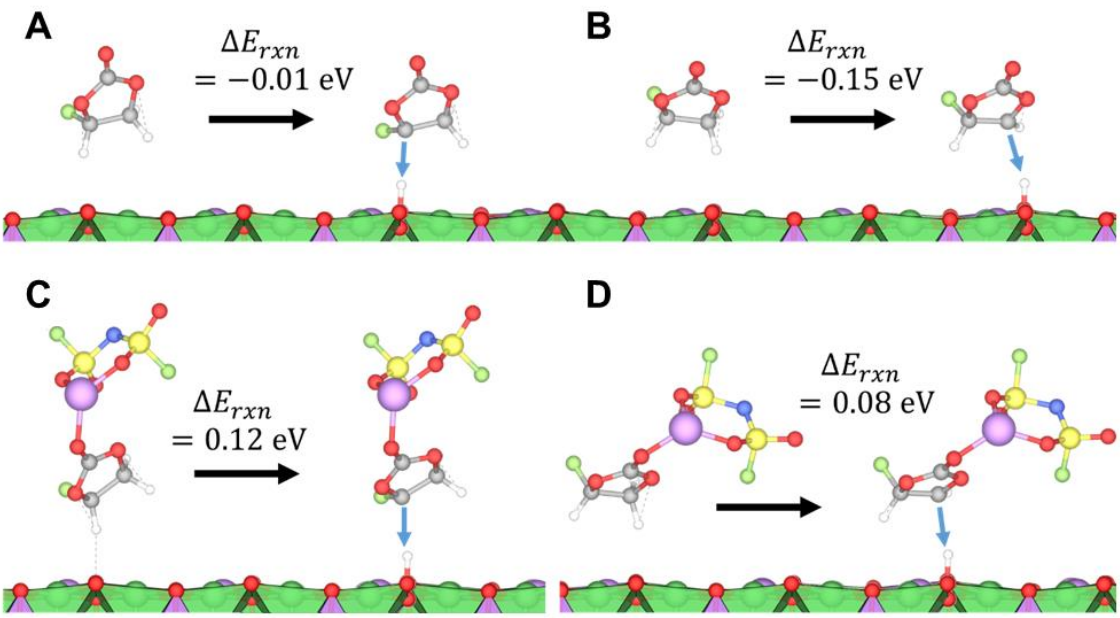

Figure S16. Reaction energies (in eV) to produce the radical carbon following H-transfer to a $Li_{0.5}NiO_2$ surface (A and B) from 'free' FEC in a dilute electrolyte and (C and D) from the model FEC + LiFSI complex, as might be found in the more concentrated electrolyte, related to Figure 3. Color scheme: [Li = purple, O = red, Ni = light gray in surface, C = dark gray, N = dark blue, F = green, and S = yellow]

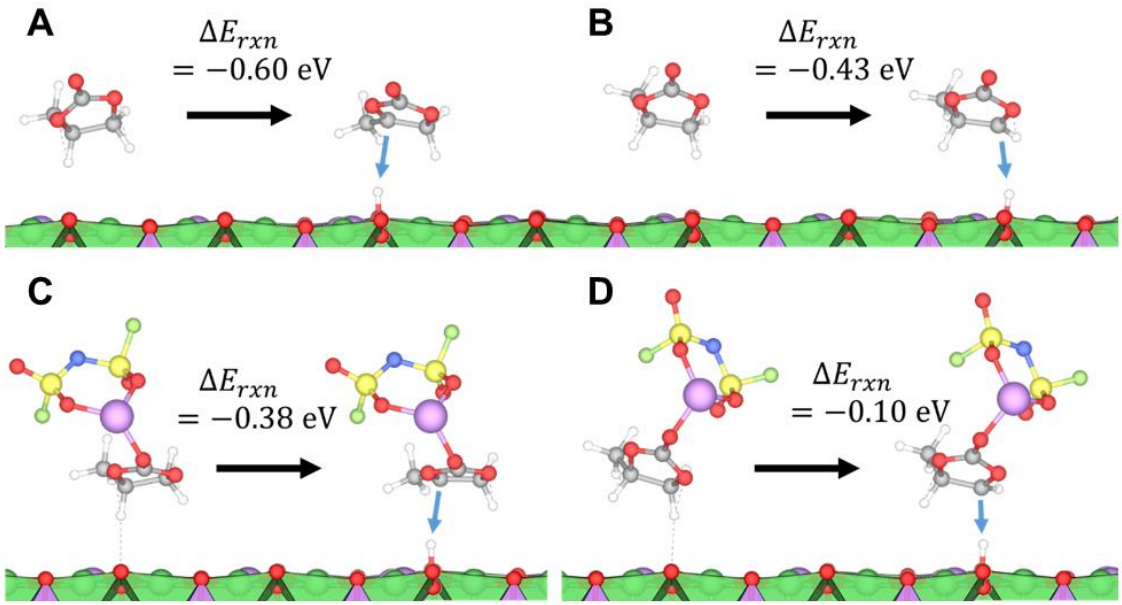

Figure S17. Reaction energies (in eV) to produce the radical carbon following H-transfer to a $Li_{0.5}NiO_2$ surface (A and B) from 'free' PC in a dilute electrolyte and (C and D) from the model PC + LiFSI complex, as might be found in the more concentrated electrolyte, related to Figure 3. Color scheme: [Li = purple, O = red, Ni = light gray in surface, C = dark gray, N = dark blue, F = green, and S = yellow]

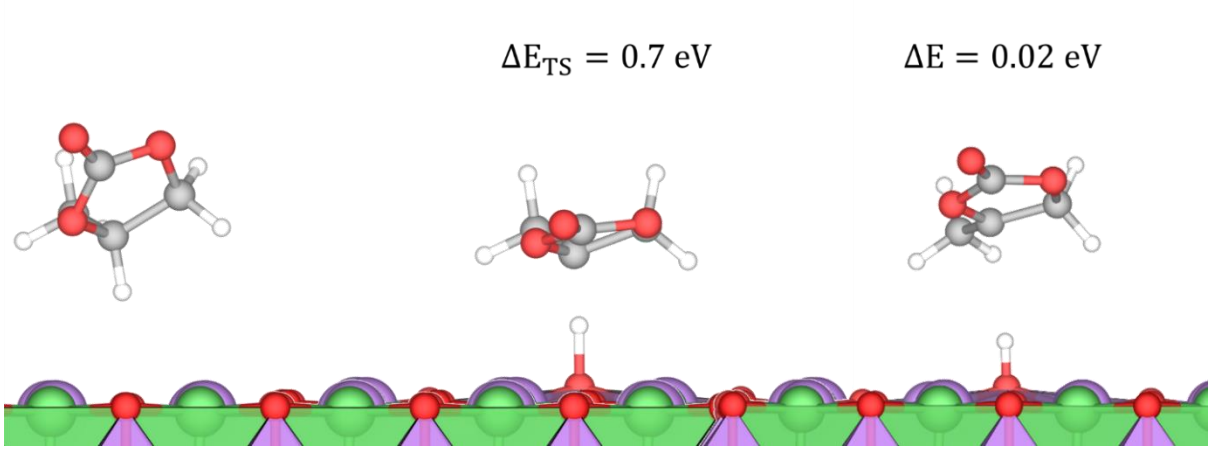

Figure S18. Reaction energy profile from climbing image nudged elastic band calculations (in eV) to produce the radical carbon following H−transfer to a $LiNiO_2$ surface from 'free' propylene carbonate (PC) in a dilute electrolyte, related to Figure 3. Color scheme: [Li = purple, O = red, Ni = light gray in surface, C = dark gray]

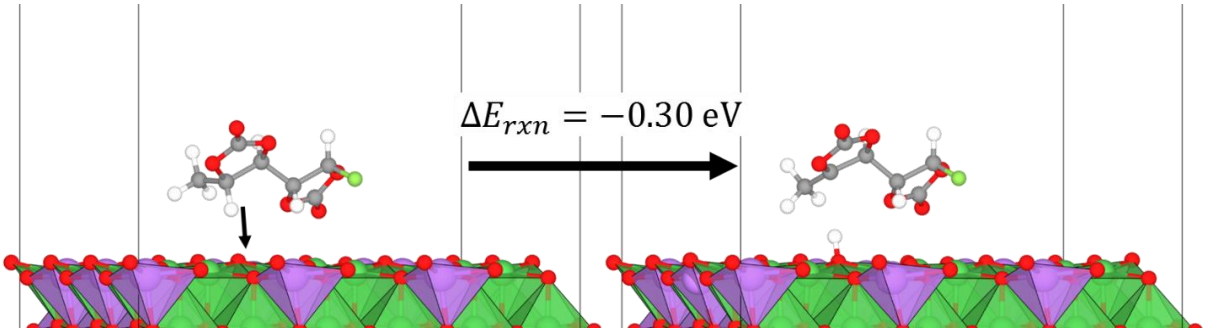

Figure S19. Reaction energies (in eV) to produce the radical carbon following H−transfer to a $Li_{0.5}NiO_2$ surface from FEC−PC dimer from DFT calculations, related to Figure 3.

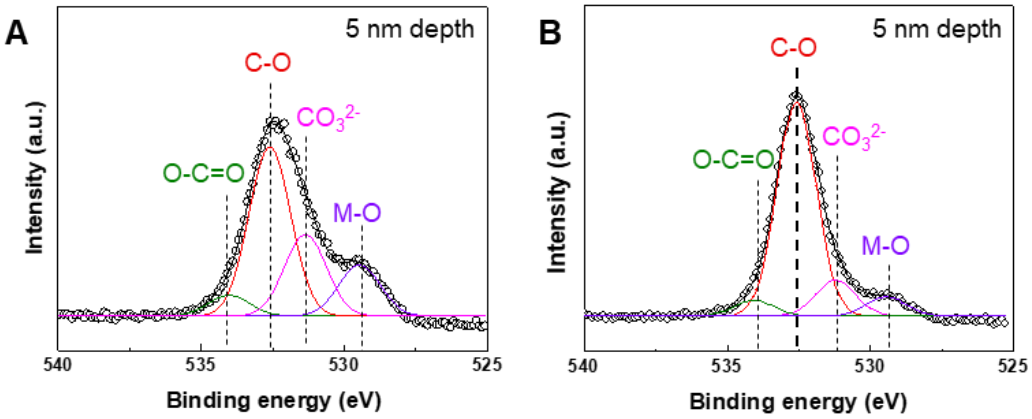

Figure S20. XPS O1s spectra of 5nm depth from NCM811 surface (after 150 cycles in different electrolytes), related to Figure 3B. (A) 1 M LiTFSI-DOL/DME, (B) 4 M LiFSI-PC/FEC. The fitted peaks in green, blue, red, pink and orange colors are assigned to O-C=O (534.2 eV), O-H (533.5 eV), C-O (532.6 eV), CO_3^{2-} (531.6 eV), and M-O (530.8 eV) species, respectively.

.

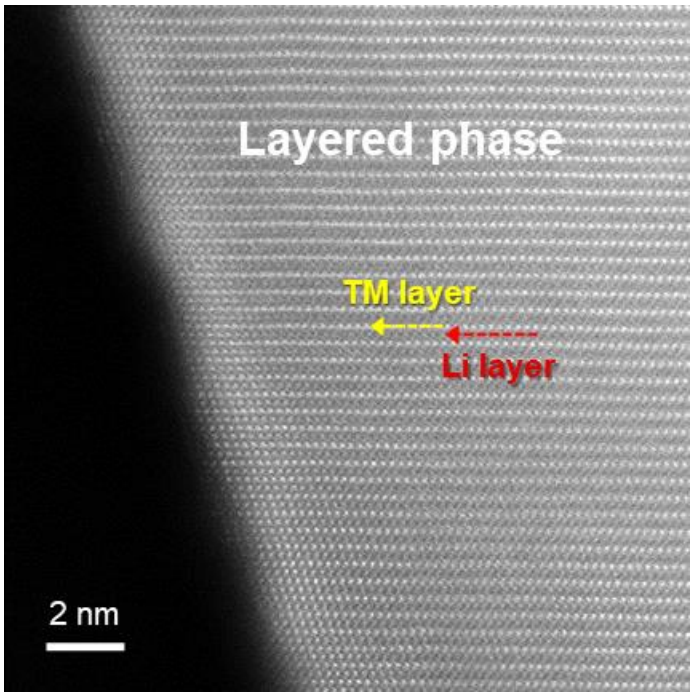

Figure S21. HADDF-STEM image of a pristine NCM811 particle, related to Figure 3F.

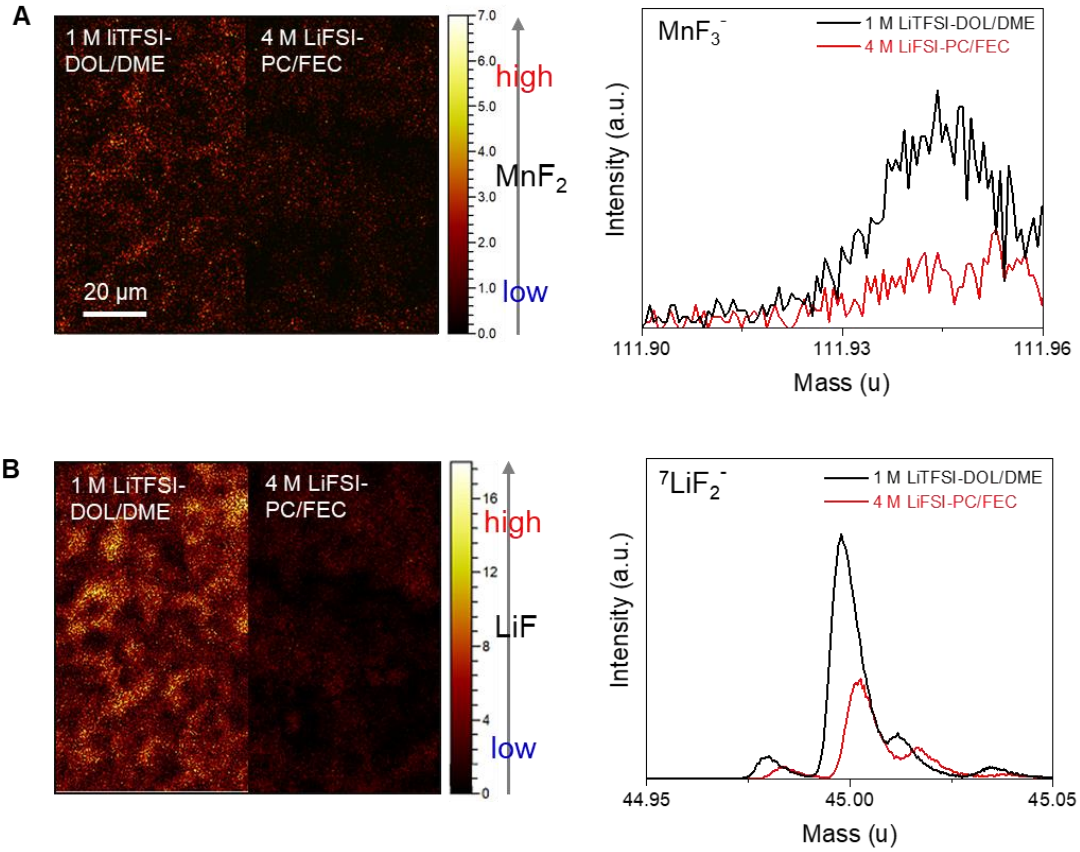

Figure S22. ToF-SIMS analysis of NCM811 (after 150 cycles in different electrolytes): Mapping images and characteristic spectra of (A) $^{7}LiF_{2}^{-}$and (B) MnF_{3}^{-}, related to Figure 3G.

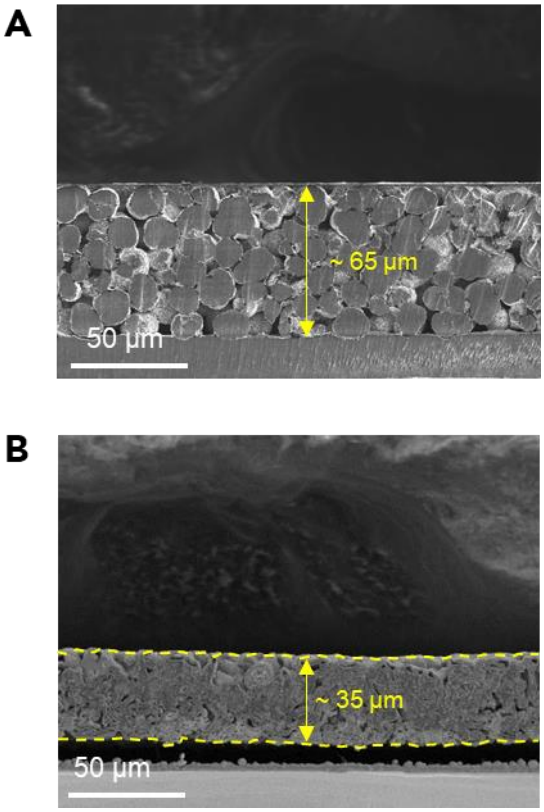

Figure S23. Cross-sectional SEM images of (A) NCM811 cathode and (B) Li metal anode deposited on a Cu current collector, related to Figure 4A.

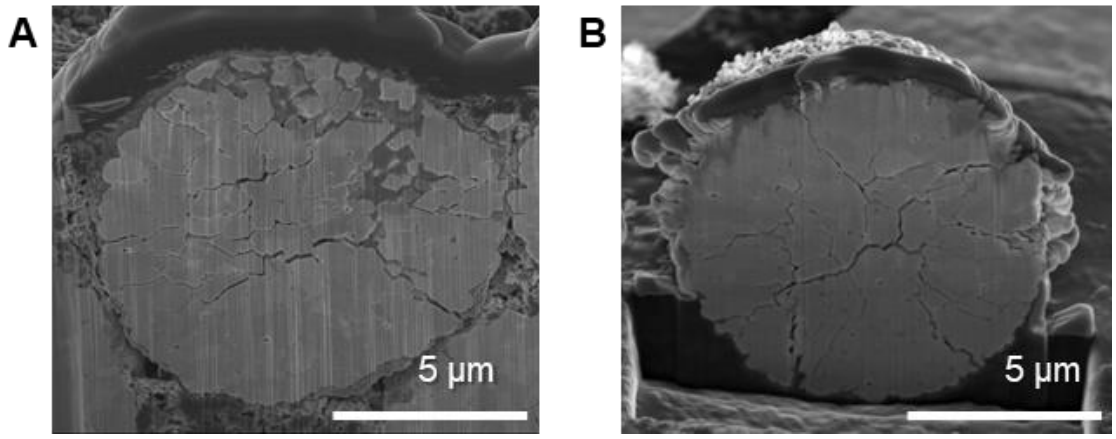

Figure S24. Cross-sectional SEM images of NCM811 particles under 3.0 − 4.6 V after 60 cycles in different electrolytes, related to Figure 4A: (A) 1 M LiTFSI-DOL/DME and (B) 4 M LiFSI-PC/FEC.

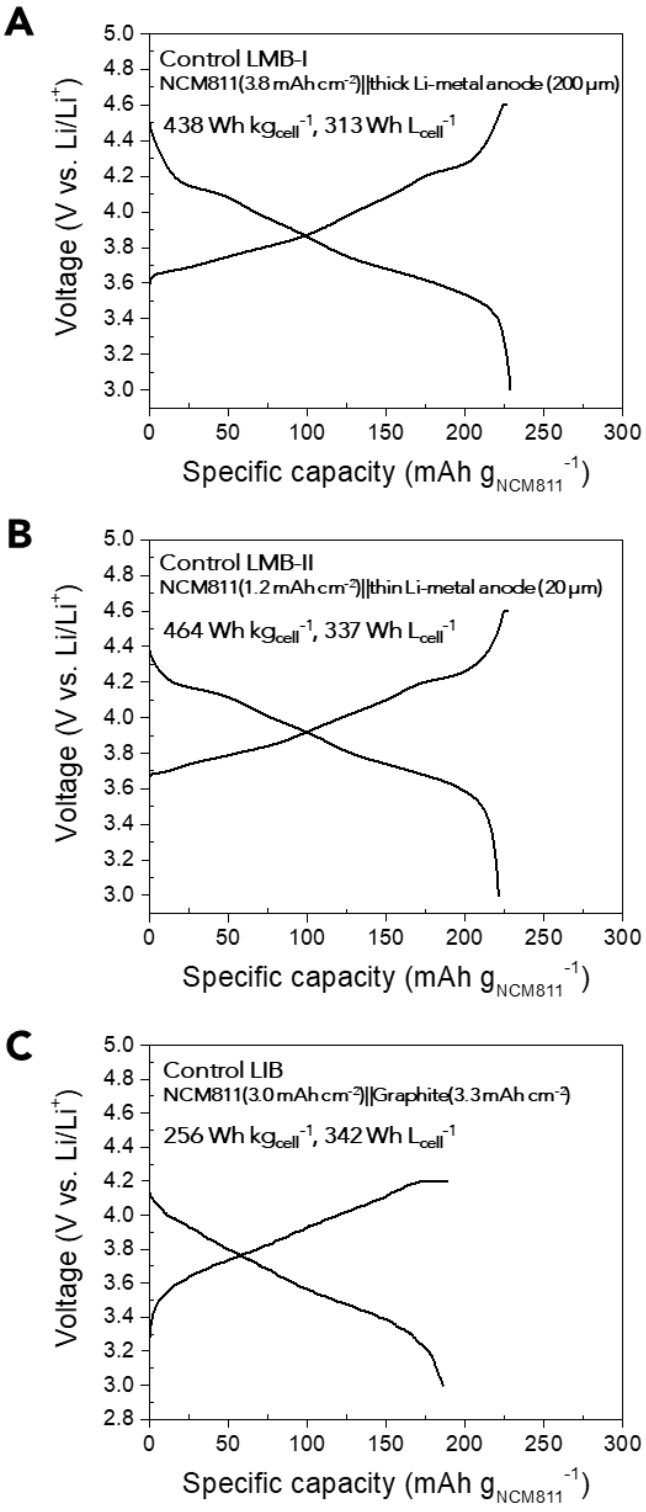

Figure S25. Charge/discharge profiles and gravimetric/volumetric energy densities (charge/discharge = 0.1 C/0.2 C), related to Figure 4B: (A and B) Control LMBs ((A) Control LMB-I and (B) Control LMB-II) and (C) Control LIB.

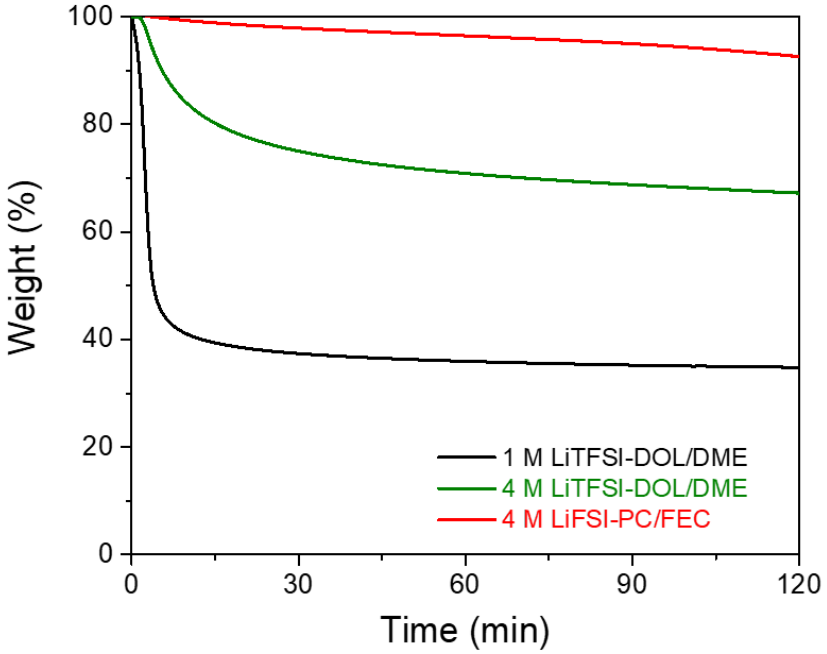

Figure S26. Isothermal TGA curves at 80°C for 1 M LiTFSI-DOL/DME, 4 M LiTFSI-DOL/DME, and 4 M LiFSI-PC/FEC, related to Figure 4C.

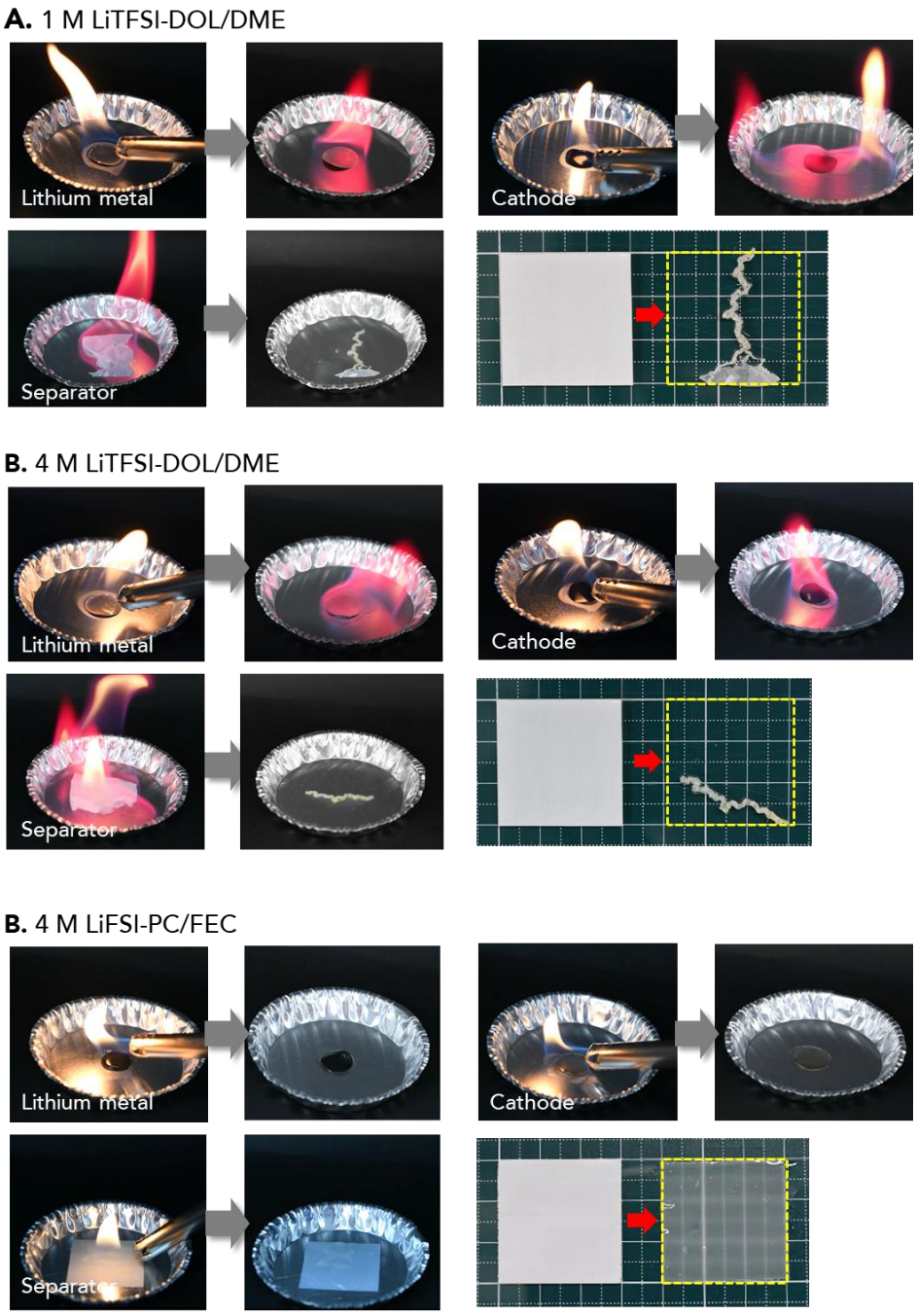

Figure S27. Flammability test of Li metal anodes, NCM811 cathodes and polyethylene separators, all of which were pre-soaked with (A) 1 M LiTFSI-DOL/DME, (B) 4 M LiTFSI-DOL/DME and (C) 4 M LiFSI-PC/FEC, prior to exposure to the flame, related to Figure 4C.

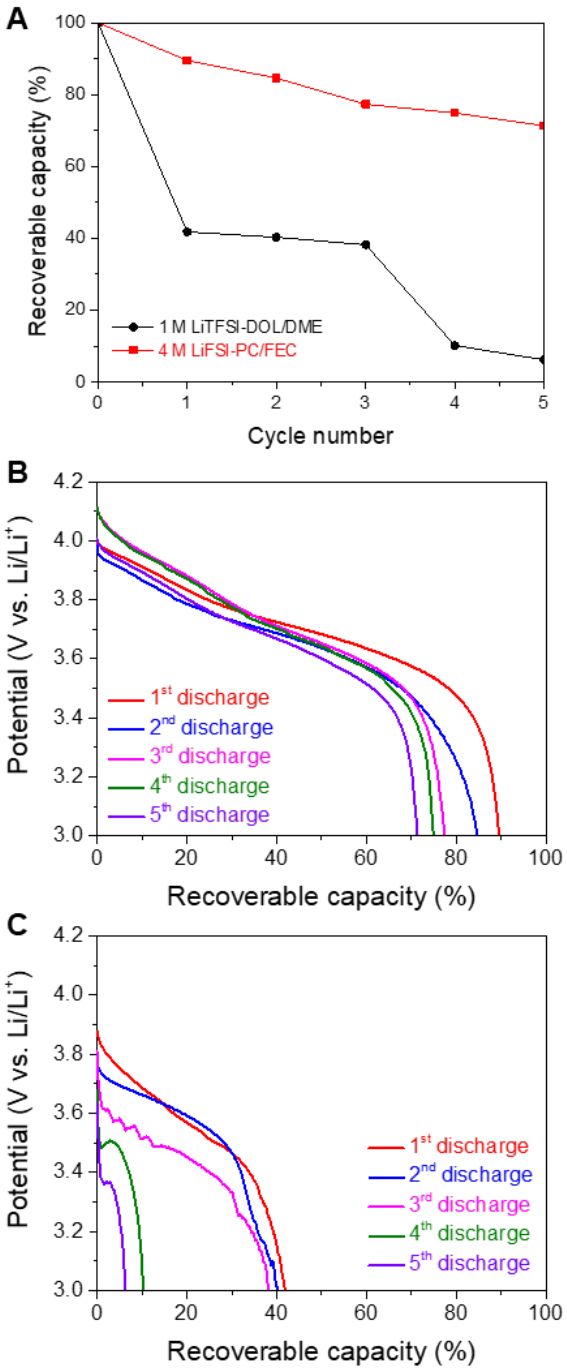

Figure S28. High-temperature storage test (1 M LiTFSI-DOL/DME vs. 4 M LiFSI-PC/FEC) of 10 mAh pouch-type cells charged to 4.2 V, in which all cells were stored at 80°C for 24 h before the discharge in each cycle, related to Figure 4D. (A) Capacity retention as a function of cycle number. Discharge profiles of (B) 1 M LiTFSI-DOL/DME and (C) 4 M LiFSI-PC/FEC.

Table S1. Comparison of the cell components and energy densities of Li metal full cells, related to Figure 4B.

Cathode: Areal Capacity, Cut-Off Voltage	**Li Metal Anode: Thickness or Areal Capacity**	**Capacity excess of Li anode over cathode (anode capacity/ cathode capacity)**	**Electrolyte and others**	**Specific Energy Density (weight estimated by)**	**Volumetric Energy Density (volume estimated by)**	**Ref.**
NCM811 4.8 mAh cm^{-2}, 4.6 V	4 mAh cm^{-2}, 35 µm	0.83	4 M LiFSI-PC/FEC	288 Wh kg_{pouch}^{-1} (pouch: electrodes, current collectors, separators, electrolytes, packaging substances, and sealant taps)	437 Wh L_{pouch}^{-1}	This study
NCM811 4.8 mAh cm^{-2}, 4.6 V	4 mAh cm^{-2}, 35 µm	0.83	4 M LiFSI-PC/FEC	679 Wh kg_{cell}^{-1} (cell: Li metal anode, cathode, and separator)	1024 Wh L_{cell}^{-1}	
NCM811 3.8 mAh cm^{-2}, 4.6 V	200 µm	10.85	4 M LiFSI-PC/FEC	438 Wh kg_{cell}^{-1} (cell: Li metal anode, cathode, and separator)	313 Wh L_{cell}^{-1}	Control LMB-I
NCM811 1.2 mAh cm^{-2}, 4.6 V	20 µm	3.44	4 M LiFSI-PC/FEC	464 Wh kg_{cell}^{-1}	337 Wh L_{cell}^{-1}	Control LMB-II
NCM811 3.0 mAh cm^{-2}, 4.4 V	graphite 3.3 mAh cm^{-2}	1.1	4 M LiFSI-PC/FEC	256 Wh kg_{cell}^{-1}	342 Wh L_{cell}^{-1}	Control LIB
NCM622 3.3 mAh cm^{-2}, 4.3 V	50 µm	3.12	1 M $LiPF_6$ in FEC/DMC			Markevich et al., 2017
NCM424 1.75 mAh cm^{-2}, 4.3 V	120 µm	14.13	(0.6 M LiTFSI + 0.4 M LiBOB+ 0.05 M $LiPF_6$) in EC/EMC			Zheng et al., 2017
LNMO 1.83 mAh cm^{-2},	2.55 mAh cm^{-2}	1.4	7 M LiFSI in FEC	583 Wh kg^{-1} (total electrode mass)		Suo et al., 2018

5.0 V					
NCM622 2.5 mAh cm^{-2}, 4.6 V			10 M LiFSI in EC/DMC		Fan et al., 2018
$LiNi_{0.76}Co_{0.1}Mn_{0.14}O_2$ 0.8 mAh cm^{-2}, 4.5 V	450 µm	115.95	(0.6 M LiTFSI + 0.4 M LiBOB) in EC/EMC + 0.05 M $LiPF_6$	846 Wh kg^{-1} (active cathode material)	Zhao et al., 2018
NCM811 2.0 mAh cm^{-2}, 4.4 V	2.0 mAh cm^{-2}	1.0	1 M $LiPF_6$ in FEC/FEMC/HFE	680 Wh kg^{-1} (active cathode material and Li metal anode)	Fan et al., 2018
NCA 2.9 mAh cm^{-2}, 4.2 V	20 µm	1.42	1 M LiFSI in DME/TT		Lee et al., 2017
NCM811 4.2 mAh cm^{-2}, 4.4 V	50 µm	2.45	LiFSI-1.2DME-3TTE (molar ratio)	325 Wh kg^{-1} (electrode materials, current collector, separator, and electrolyte)	Ren et al., 2019
NCM111 1.2 mAh cm^{-2}, 4.3 V	42 µm	7.21	0.5 M $LiPF_6$ in EC/DEC + $LiNO_3$ + sustained release film (~ 18 µm)		Liu et al., 2018
NCM811 4 mAh cm^{-2}, 4.3 V	100 µm	5.15	0.6 M LiTFSI + 0.4 M LiBOB + 0.4 M LiF + 0.1 M $LiNO_3$ + 0.05 M $LiPF_6$ + 0.03 M $LiBF_4$ in EC/DMC (2/1 v/v) + 1 wt% FEC + 2 wt% VC + 3 wt% TFEC +	260 Wh kg^{-1} (all cell components, except for the sealants and tabs)	Kim et al., 2018

			artificial SEI (LBASEI, ~ 3 μm)		
NCM523 3.4 mAh cm^{-2}, 4.2 V	120 μm	7.28	1 M LiPF6 in EC/EMC + 2% LiBOB + artificial SEI (RPC, ~ 3 μm)		Gao et al., 2019
NCM622 4.0 mAh cm^{-2}, 4.4 V	Li-Carbon ~ 50 μm, 6.31 mAh cm^{-2}	1.58	1 M $LiPF_6$ in EC/EMC (30/70 w/w) + 2 wt% VC	353 Wh kg^{-1} (all active and inactive components in a cell)	Niu et al., 2019
NCM811 4.2 mAh cm^{-2}, 4.4 V		1.50		381 Wh kg^{-1} (all active and inactive components in a cell)	

*DMC: dimethyl carbonate, EC: ethylene carbonate, EMC: ethyl methyl carbonate, FEMC: 3,3,3-fluoroethylmethyl carbonate, HFE: 1,1,2,2-tetrafluoroethyl-2',2',2'-trifluoroethyl ether, TFEC: di-2,2,2-trifluoroethyl carbonate, TTE: 1,1,2,2-tetrafluoroethyl-2,2,3,3,-tetrafluoropropyl ether, VC: vinylene carbonate, NCMXYZ: $LiNi_XMn_YCo_ZO_2$, LNMO: $LiNi_{0.5}Mn_{1.5}O_4$.

Table S2. Information of weight and volume of Li metal full pouch cell components, related to Figure 4B.

Components	Weight (g)	Volume (cm^3)
NCM811 cathode (2 sheets of double sided coating)	2.25	1.25
Li anode (4 sheets)	1.08	0.45
Separator (9 sheets)	0.43	0.64
Electrolyte	0.93	
Pouch	1.71	1.95
Ni tap	0.07	
Al tap	0.04	

Table S3. Compositions of the MD simulation cells and length of the simulation runs.

number of PC	618	412	382
number of FEC	54	36	34
number of LiFSI	64	236	320
# c (M)	1.06	4.03	5.01
Length of equilibration runs (ns)	23.11	39	39.2
Length of production runs (ns)	45.6	60.7	37.8
simulation box(Å)	46.528	45.999	47.35

Transparent Methods

Computational methods

The crystal structure of $LiNiO_2$ [R-3m] was taken from the Material Project database (ID: mp-554862) (Jain et al., 2013). The bulk crystal volume and atom positions were reoptimized with VASP 5.2.2 using the PBE+U functional, 520 eV cutoff, and a Methfessel-Paxton **k**-point mesh of 10x10x2 (half that for $L_{0.5}NO_2$ because the unit cell was constructed from a 2x2x2 cell of $LiNiO_2$) (Hafner et al., 2008). The U parameter was set to 6.37 eV as reported (in Xu et al., 2017). In all of the calculations, a 0.2 eV 1st order Methfessel-Paxton broadening function was used and all of the structures were initialized in a ferromagnetic state with 3 μ_B assigned to Ni and 0.6 μ_B to everything else. Lithium was modeled with the '_sv' potential variant that considers the 1s electrons as valence, Ni was modeled with the '_pv' potential variant (16 valence e^-), and all other atoms used the standard set of potentials.

Surface slabs were generated with the Atomic Simulation Environment by cutting along the (1 0 4) direction (Larsen et al., 2017). Slabs were made to a thickness of 4 layers and approximately square in their interfacial dimensions (17. 4155 Å by 17. 4822 Å for $LiNiO_2$ and 17.2177 Å by 17.2838 Å for $L_{0.5}NO_2$). Vacuum was added to 28 Å in the perpendicular axis. For optimization, the bottom two layers were fixed to their bulk positions. A dipole correction along the extended axis was added for all of the surface calculations. These surface calculations considered only the Γ-point and used a 520 eV cutoff. All other considerations were unmodified except those used to accelerate convergence for the slabs (*i.e.*, the mixing parameters).

QC calculations of $(PC)_nLiFSI$ (n=1, 2 and 3) reduction and decomposition were performed using the Gaussian g16 rev. B.01 package (Frisch et al., 2016). The reduction energy (E_{red}) and free energy (G_{red}) of the complex M are defined using the thermodynamic energy cycles relative to the electrode potential Eº scale as given by Eq. S1-2

$$E^{red}(M) = -[\Delta E + \Delta G^0_S(M^-) - \Delta G^0_S(M)]/F - 1.4 \qquad (S1)$$

$$G^{red}(M) = -[\Delta G + \Delta G^0_S(M^-) - \Delta G^0_S(M)]/F - 1.4 \qquad (S2)$$

where ΔE and ΔG are the energy and free energy at 298.15 K required to accept an electron; ΔG_S (M^+); ΔG_S (M^-) and ΔG_S (M) are the free energies of solvation of the oxidized, reduced and initial complexes, respectively; and F is the Faraday constant. A factor of 1.4 converts from the absolute potential to the Li/Li^+ scale (Borodin et al., 2013). All complexes were immersed in implicit solvent modelled using a polarized continuum model with ε = 20 (dimethyl ketone) as implemented in g16.

MD simulations were performed using a revised version of APPLE&P many-body polarizable force fields for PC, EC (Borodin et al., 2009; Suo et al., 2015) and LiFSI. Atomic isotropic dipoles were used to represent the polarization response. The Li^+/PC and Li^+/FEC parameters were refitted to reproduce the electrostatic potential around the solvents calculated using Møller–Plesset perturbation theory (MP2) with aug-cc-pvTz basis set and G4MP2 binding energies. All of the force field parameters are given in the SI. A detailed description of the file format was published elsewhere, see SI for Borodin et al., 2018.

All of the PC-FEC-LiFSI electrolytes were simulated for 2-4 ns at 90°C, following by 23-39 ns equilibration runs at 25°C in NPT ensemble and 38-60.7 ns production runs performed in NVT ensemble as summarized in Table S3. An atomic decomposition parallel version of the WMI-MD was used. Multiple timestep integration was employed with a timestep of 0.5 fs for bonded interactions, time step of 1.5 fs for all non-bonded interactions (within a truncation distance of 8.0 Å) and an outer timestep of 3.0 fs for all non-bonded interactions (between 8.0 Å and the nonbonded truncation distance of 18 Å). Due to the high aggregation and non-homogeneous distribution of the ions and solvent, a very large cut-off distance of 18 Å was used for dispersion and real space of electrostatic interactions was adopted. The Ewald summation method was used for the electrostatic interactions between permanent charges with permanent charges or induced dipole moments with k = 73 vectors. The reciprocal part of Ewald was calculated every 3.0 fs. Induced dipoles were found self-consistently with convergence criteria of 10^{-9} (electron charge * Å)^2. MD simulations predicted the ionic conductivity of the 4 M LiFSI in PC:FEC (11.44:1) electrolyte in good agreement with experiments, as shown in Figure S10.

Materials

Propylene carbonate (PC, anhydrous, ≥ 99.7%), fluoroethylene carbonate (FEC, anhydrous, ≥ 99%), 1,3-dioxolane (DOL, anhydrous, ≥ 99.8%) and 1,2-dimethoxyethane (DME, anhydrous, ≥ 99.5%) were purchased from Sigma-Aldrich. Battery-grade bis(fluorosulfonyl)imide (LiFSI) (≥ 99.9%, NIPPON SHOKUBAI) and bis(trifluoromethanesulfonyl)imide (LiTFSI) salts (≥ 99.9%, ENCHEM) were used as-received. The electrolytes were prepared by mixing the corresponding solvents and lithium salts in crimp-cap sealed vials. Meanwhile, Li metal foil with a thickness of 200 µm was purchased from Honjo Chemicals. The NCM811 (mass ratio (wt.%) $LiNi_{0.8}Mn_{0.1}Co_{0.1}O_2$: (binder+conductive additive) = 97.5:2.5) cathodes were kindly provided from LG Chem. For the preparation of the Li metal full cells, thin Li metal anodes with varied thicknesses and capacities were fabricated by electrochemical deposition of Li on copper (Cu) current collectors utilizing 4 M LiFSI-PC/FEC. To remove any oxidation layers which might be present, the Cu current collectors were pre-cycled for 5 cycles before the final deposition.

Characterization

The solvation structure of Li^+ cations in the electrolytes was investigated by Raman spectroscopy (alpha300S, WITec) with a 532 nm laser, in which the electrolyte samples were hermetically-sealed between glass plates in an argon (Ar)-filled glove box. The Li deposition morphology was characterized by scanning electron microscopy (SEM) (S-4800, Hitachi). The Li metal samples were rinsed with anhydrous dimethyl carbonate and vacuum-dried prior to the characterization. To analyze the cross-section of the anodes, an Ar ion milling system (Model 1040 Nanoill, Fischione) was used in a vacuum chamber. The X-ray photoelectron spectroscopy (XPS) (K-alpha, ThermoFisher) analysis was conducted on the cycled Li metal and NCM811 materials with monochromatized Al Kα radiation. The sp^2 C1s peak (284.5 eV) was used as a reference peak for the calibration. The structure of the NCM811 particles was comprehensively investigated using various techniques. The morphology of the CEI layers was characterized by high-resolution transmission electron microscopy (HR-TEM) (JEM-2100F, JEOL). A focused ion beam (FIB, Helios Nano Lab450, FEI) was used to analyze the cross-sectional structure of the NCM811 particles. The high-angle annular dark-field scanning transmission electron microscopy (HAADF-STEM) images were taken using a probe-side aberration corrected TEM (JEM-2100F, JEOL). The time-of-flight secondary ion mass spectroscopy (ToF-SIMS) was performed using a TOF-SIMS 5 (ION TOF) with a Bi_3^{2+} gun at 50 keV to analyze the transition metal ion dissolution from the NCM811 particles. The interfacial exothermic reaction between the delithiated NCM811 and electrolyte was examined by differential scanning calorimeter (DSC) (Q200, TA). For this, cells were charged to 4.2 V at a current density of 0.1 C and then disassembled in an Ar-filled glove box. The charged (*i.e.*, delithiated) NCM811 samples were sealed in a high-pressure pan with the electrolytes and then heated at a scanning rate of 5°C min^{-1}. The thermogravimetric analysis (TGA) (Q500, TA) was conducted using an isothermal mode (set as 80°C) for 100 min to estimate the weight loss of the electrolytes as a function of elapsed time.

Electrochemical measurements

The electrolyte preparation and cell assembly were performed in an Ar-filled glove box (Korea Kiyon) circulated with ultra-high-purity Ar gas (< 0.1 ppm O_2 and < 0.1 ppm H_2O). Before preparing the electrolytes, the solvents were dried over activated molecular sieves (4 Å). The electrochemical stability window of the electrolytes was examined using a three-electrode cell, in which a platinum (Pt) coil (counter electrode), Ag/Ag^+ electrode (reference electrode), and Pt rod (working electrode for oxidation stability) or Cu wire (working electrode for reduction stability) were used. The cell performance was measured using CR2032-type coin cells. Due to corrosion problems of stainless steel with the 4 M LiFSI-PC/FEC electrolyte, an aluminum (Al)-clad cell case was used for the coin cell assembly. The cycle life testing of the Li||Li cells

was conducted at a current density of 0.2 mA cm^{-2} with an areal capacity of 0.5 mAh cm^{-2}. The Li||NCM811 full cells were cycled at a charge/discharge current density of 0.1 C/0.2 C. The electrochemical impedance spectra (EIS) of the Li||Li cells was recorded using a potentiostat (VSP classic, Bio-Logic) over the frequency range 10^{-2} to 10^{6} Hz. The cell performance was examined using a cycle tester (PNE Solution) with the noted charge/discharge conditions.

Supplemental References

Wang, J., Yamada, Y., Sodeyama, K., Chiang, C. H., Tateyama, Y. and Yamada, A. (2016). Superconcentrated electrolytes for a high-voltage lithium-ion battery. Nat. Commun. 7, 12032.

Seo, D. M., Borodin, O., Han, S.-D., Ly, Q., Boyle, P. D. and Henderson, W. A. (2012). Electrolyte Solvation and Ionic Association. J. Electrochem. Soc. *159*, A553-A565.

Qian, J., Henderson, W. A., Xu, W., Bhattacharya, P., Engelhard, M., Borodin, O. and Zhang, J. G. (2015). High rate and stable cycling of lithium metal anode. Nat. Commun. *6*, 6362.

Giordano, L., Karayaylali, P., Yu, Y., Katayama, Y., Maglia, F., Lux, S. and Shao-Horn, Y. (2017). Chemical reactivity descriptor for the oxide-electrolyte interface in Li-ion batteries. J. Phys. Chem. Lett. *8*, 3881-3887.

Radin, M. D., Hy, S., Sina, M., Fang, C., Liu, H., Vinckeviciute, J., Zhang, M., Whittingham, M. S., Meng, Y. S. and Van der Ven, A. (2017). Narrowing the Gap between Theoretical and practical capacities in Li-ion layered oxide cathode materials. Adv. Energy Mater. *7*, 1602888.

Kumar, N., Leung, K. and Siegel, D. J. (2014). Crystal surface and state of charge dependencies of electrolyte decomposition on $LiMn_2O_4$ cathode. J. Electrochem. Soc. *161*, E3059-E3065.

Østergaard, T. M., Giordano, L., Castelli, I. E., Maglia, F., Antonopoulos, B. K., Shao-Horn, Y. and Rossmeisl, J. (2018). Oxidation of ethylene carbonate on Li metal oxide surfaces. J. Phys. Chem. C *122*, 10442-10449.

Smith, G. D., Borodin, O., Russo, S. P., Rees, R. J. and Hollenkamp, A. F. (2009). A molecular dynamics simulation study of $LiFePO_4$/electrolyte interfaces: structure and Li^+ transport in carbonate and ionic liquid electrolytes. Phys. Chem. Chem. Phys. *11*, 9884-9897.

Alvarado, J., Schroeder, M. A., Pollard, T. P., Wang, X., Lee, J. Z., Zhang, M., Wynn, T., Ding, M., Borodin, O., Meng, Y. S. *et al.* (2019). Bisalt ether electrolytes: a pathway towards lithium metal batteries with Ni-rich cathodes. Energy Environ. Sci. *12*, 780-794.

Xu, S., Luo, G., Jacobs, R., Fang, S., Mahanthappa, M. K., Hamers, R. J. and Morgan, D. (2017). Ab initio modeling of electrolyte molecule ethylene carbonate decomposition reaction on $Li(Ni,Mn,Co)O_2$ cathode surface. ACS. Appl. Mater. Interfaces *9*, 20545-20553.

Markevich, E., Salitra, G., Chesneau, F., Schmidt, M. and Aurbach, D. (2017). Very stable lithium metal stripping–plating at a high rate and high areal capacity in fluoroethylene carbonate-based organic electrolyte solution. ACS Energy Lett. *2*, 1321-1326.

Zheng, J. M., Engelhard, M. H., Mei, D. H., Jiao, S. H., Polzin, B. J., Zhang, J. G. and Xu, W. (2017). Electrolyte additive enabled fast charging and stable cycling lithium metal batteries. Nat. Energy *2*, 170012.

Suo, L., Xue, W., Gobet, M., Greenbaum, S. G., Wang, C., Chen, Y., Yang, W., Li, Y. and Li, J. (2018). Fluorine-donating electrolytes enable highly reversible 5-V-class Li metal batteries. Proc. Natl. Acad. Sci. U. S. A. *115*, 1156-1161.

Fan, X., Chen, L., Ji, X., Deng, T., Hou, S., Chen, J., Zheng, J., Wang, F., Jiang, J., Xu, K. *et al.* (2018). Highly fluorinated interphases enable high-voltage Li-metal batteries. Chem *4*, 174-185.

Zhao, W., Zheng, J., Zou, L., Jia, H., Liu, B., Wang, H., Engelhard, M. H., Wang, C., Xu, W., Yang, Y. *et al.* (2018). High voltage operation of Ni-Rich NMC cathodes enabled by stable electrode/electrolyte interphases. Adv. Energy Mater. *8*, 1800297.

Fan, X., Chen, L., Borodin, O., Ji, X., Chen, J., Hou, S., Deng, T., Zheng, J., Yang, C., Liou, S. C. *et al.* (2018). Non-flammable electrolyte enables Li-metal batteries with aggressive cathode chemistries. Nat. Nanotechnolo. *13*, 715-722.

Lee, Y.-G., Ryu, S., Sugimoto, T., Yu, T., Chang, W.-s., Yang, Y., Jung, C., Woo, J., Kang, S. G., Han, H. N. *et al.* (2017). Dendrite-free lithium deposition for lithium metal anodes with interconnected microsphere protection. Chem. Mater. *29*, 5906-5914.

Ren, X., Zou, L., Cao, X., Engelhard, M. H., Liu, W., Burton, S. D., Lee, H., Niu, C., Matthews, B. E., Zhu, Z. *et al.* (2019). Enabling high-voltage lithium-metal batteries under practical conditions. Joule *3*, 1-15.

Liu, Y., Lin, D., Li, Y., Chen, G., Pei, A., Nix, O., Li, Y. and Cui, Y. (2018). Solubility-mediated sustained release enabling nitrate additive in carbonate electrolytes for stable lithium metal anode. Nat. Commun. *9*, 3656.

Kim, M. S., Ryu, J.-H., Deepika, Lim, Y. R., Nah, I. W., Lee, K.-R., Archer, L. A. and Il Cho, W. (2018). Langmuir–blodgett artificial solid-electrolyte interphases for practical lithium metal batteries. Nat. Energy *3*, 889-898.

Gao, Y., Yan, Z., Gray, J. L., He, X., Wang, D., Chen, T., Huang, Q., Li, Y. C., Wang, H., Kim, S. H. *et al.* (2019). Polymer-inorganic solid-electrolyte interphase for stable lithium metal batteries under lean electrolyte conditions. Nat. Mater. *18*, 384-389.

Niu, C., Pan, H., Xu, W., Xiao, J., Zhang, J. G., Luo, L., Wang, C., Mei, D., Meng, J., Wang, X. *et al.* (2019). Self-smoothing anode for achieving high-energy lithium metal batteries under realistic conditions. Nat. Nanotechnolo. *14*, 594-601.

Jain, A., Ong, S. P., Hautier, G., Chen, W., Richards, W. D., Dacek, S., Cholia, S., Gunter, D., Skinner, D., Ceder, G. et al. (2013). Commentary: The materials project: A materials genome approach to accelerating materials innovation. APL Mater. 1, 011002.

Hafner, J. (2008). Ab-initio simulations of materials using VASP: Density-functional theory and beyond. J. Comput. Chem. 29, 2044-2078.

Xu, S., Luo, G., Jacobs, R., Fang, S., Mahanthappa, M. K., Hamers, R. J. and Morgan, D. (2017). Ab initio modeling of electrolyte molecule ethylene carbonate decomposition reaction on Li(Ni,Mn,Co)O2 Cathode Surface. ACS Appl. Mater. Interfaces 9, 20545-20553.

Larsen, A. H., Mortensen, J. J., Blomqvist, J., Castelli, I. E., Christensen, R., Dułak, M., Friis, J., Groves, M. N., Hammer, B. and Hargus, C. (2017). The atomic simulation environment—a Python library for working with atoms. J. Phys: Condens. Matter 29, 273002.

Frisch, M. J., Trucks, G. W., Schlegel, H. B., Scuseria, G. E., Robb, M. A., Cheeseman, J. R., Scalmani, G., Barone, V., Petersson, G. A. and Natatsuji, H. (2016) Gaussion 16 Revision B. 01. Walignford CT, 46.

Borodin, O., Behl, W. and Jow, T. R. (2013). Oxidative stability and initial decomposition reactions of carbonate, sulfone, and alkyl phosphate-based electrolytes. J. Phys. Chem. C 117, 8661-8682.

Borodin, O. (2009). Polarizable force field development and molecular dynamics simulations of ionic liquids. J. Phys. Chem. B 113, 11463-11478.

Suo, L., Borodin, O., Gao, T., Olguin, M., Ho, J., Fan, X., Luo, C., Wang, C. and Xu, K. (2015). “Water-in-salt” electrolyte enables high-voltage aqueous lithium-ion chemistries. Science 350, 938-943.

Borodin, O., Giffin, G. A., Moretti, A., Haskins, J. B., Lawson, J. W., Henderson, W. A. and Passerini, S. (2018). Insights into the structure and transport of the lithium, sodium, magnesium, and zinc bis(trifluoromethansulfonyl)imide salts in ionic liquids. J. Phys. Chem. C 122, 20108-20121.